

The stellar halo of isolated central galaxies in the Hyper Suprime-Cam imaging survey

Wenting Wang^{1*}, Jiaxin Han^{2,1}, Alessandro Sonnenfeld^{3,1}, Naoki Yasuda¹, Xiangchong Li¹, Yipeng Jing², Surhud More^{4,1}, Paul A. Price⁵, Robert Lupton⁵, David V. Stark¹, Ting-Wen Lan¹, Masahiro Takada¹, Song Huang⁶, Wentao Luo¹, Neta A. Bahcall⁵, Yutaka Komiyama^{7,8}

¹ *Kavli IPMU (WPI), UTIAS, The University of Tokyo, Kashiwa, Chiba 277-8583, Japan*

² *Department of Astronomy, Shanghai Jiao Tong University, Shanghai 200240, China*

³ *Leiden Observatory, Leiden University, Niels Bohrweg 2, 2333 CA Leiden, the Netherlands*

⁴ *The Inter-University Centre for Astronomy and Astrophysics, Post bag 4, Ganeshkhind, Pune 411007, India*

⁵ *Department of Astrophysical Sciences, Princeton University, 4 Ivy Lane, Princeton, NJ08544, USA*

⁶ *Department of Astronomy and Astrophysics, University of California Santa Cruz, 1156 High St., Santa Cruz, CA 95064, USA*

⁷ *National Astronomical Observatory of Japan, 2-21-1 Osawa, Mitaka, Tokyo 181-8588, Japan*

⁸ *Graduate University for Advanced Studies (SOKENDAI), 2-21-1 Osawa, Mitaka, Tokyo 181-8588, Japan*

21 July 2022

ABSTRACT

We study the faint stellar halo of isolated central galaxies, by stacking galaxy images in the HSC survey and accounting for the residual sky background sampled with random points. The surface brightness profiles in HSC r -band are measured up to 120 kpc from the galaxy center for a wide range of galaxy stellar mass ($9.2 < \log_{10} M_*/M_\odot < 11.4$), and down to a surface brightness of about $32.8 \text{ mag/arcsec}^2$, with an indication of signals to even larger scales and fainter magnitudes. Failing to account for the outer stellar halo below the noise level of individual images will lead to underestimates of the total luminosity by $\leq 20\%$. Splitting galaxies according to the concentration parameter of their light distributions, we find that the surface brightness profiles of low concentration galaxies drop faster between 20 kpc and 100 kpc and are more extended beyond 100 kpc than those of high concentration galaxies. The profiles of low concentration galaxies persist out to the average halo virial radius. Albeit the large galaxy-to-galaxy scatter, we find a strong self-similarity of the stellar halo profiles. They show unified forms once the projected distance is scaled by the halo virial radius. The colour of the stellar halo is redder in the center and bluer outside, with high concentration galaxies having redder and flatter colour profiles. Such a colour gradient persists to about 80 kpc for galaxies more massive than $10^{10.2} M_\odot$, whereas for galaxies with $9.2 < \log_{10} M_*/M_\odot < 10.2$, the gradient is consistent with being flat between 10 kpc and 30 kpc.

Key words: Galaxy: halo - dark matter

1 INTRODUCTION

In the current structure formation paradigm of Λ CDM, galaxies form by the cooling and condensation of gas at centres of an evolving population of dark matter haloes (White & Rees 1978). Dark matter haloes grow in mass and size through both smooth accretion of diffuse matter and from mergers with other haloes spanning a very wide range in mass (e.g. Wang et al. 2011). Smaller haloes having their

own central galaxies fall into larger haloes and become “sub-haloes” and “satellites” of the galaxy at the centre of the dominant host halo. Orbiting around the central galaxy and undergoing tidal stripping, these satellites and subhaloes lose their mass. Stripped stars form stellar streams, which then gradually mix in phasespace afterwards, losing their own binding energy and sinking to the center due to dynamical frictions. These stars form the diffuse light or the faint stellar halo around the central galaxy (e.g. Bullock & Johnston 2005; Cooper et al. 2010). In the end, satellite galaxies

* wenting.wang@ipmu.jp, bilinxing.wenting@gmail.com

and stripped material from these satellites merge with the central galaxy and contribute to its growth.

With the advent of large telescopes and deep imaging, galaxy stellar haloes and the connection to galaxy mergers in both our Milky Way and nearby individual galaxies have been detected and studied (e.g. Schweizer 1980; Malin & Carter 1983; Schweizer & Seitzer 1992; Mihos et al. 2005; Tal et al. 2009; Martínez-Delgado et al. 2010; van Dokkum et al. 2014; Greggio et al. 2018; Ann & Park 2018). Tidal structures have been observed in individual galaxies, which supports the above structure formation paradigm. In particular, for our Milky way and very nearby disk and lenticular galaxies, the stellar population can be resolved and the stellar halo can be studied through star counts (e.g. Bell et al. 2008; Monachesi et al. 2013; Ibata et al. 2014; Peacock et al. 2015; Staudaher et al. 2015).

The intensity or surface brightness, I , of extended objects drops with distance, in a relationship with redshift, z , as $I \propto (1+z)^{-4}$. Hence for more distant galaxies, their faint stellar haloes can be only a few percent or even less of the sky background. This makes the study of distant and individual stellar haloes relatively difficult, but with deep exposures on large telescopes, it is becoming possible and common to look at the outer stellar halo, tidal structures and mass accretion through cosmic time for massive individual galaxies at intermediate ($z \sim 0.4$) and even higher redshifts ($z \sim 1$) (e.g. Buitrago et al. 2017; Huang et al. 2018a,b; Kado-Fong et al. 2018).

Alternatively, images of a large sample of galaxies with similar properties can be stacked together to achieve the average extended light distribution of galaxies (e.g. Zibetti et al. 2004, 2005; Tal & van Dokkum 2011; D’Souza et al. 2014). Although stacking smooths out delicate structures and the fine shape of galaxies, it is a powerful approach that enables studying the averaged smooth light distribution of the faint stellar haloes for more distant galaxies, and the stacked surface brightness profiles can be measured for galaxies spanning a wide range of luminosity/stellar mass, covering those smaller than the Milky Way ($\log_{10} M_*/M_\odot \sim 10$) to massive cD galaxies of groups and clusters.

Theoretical studies on the formation of extended stellar haloes involve a few different approaches including analytical models (e.g. Purcell et al. 2007), numerical simulations (e.g. Oser et al. 2010; Lackner et al. 2012; Pillepich et al. 2014; Rodríguez-Gomez et al. 2016; Karademir et al. 2018) and semi-analytical approaches of particle painting/tagging method (e.g. Cooper et al. 2013, 2015). In these studies, it is demonstrated that galaxy formation involves two phases, an early rapid formation of “in-situ” stars through gas cooling and a later phase of mass growth through accretion of smaller satellite galaxies. Accreted stellar material typically lies in the outskirts of galaxies and are more metal poor than “in-situ” stars. The fraction of accreted stellar mass with respect to the total mass of galaxies is higher for more massive galaxies and for elliptical galaxies. These results are generally consistent with existing observations.

Recently, using the Hyper Suprime-Cam Subaru Strategic Program Survey deep coadd imaging data, Huang et al. (2018a) looked at the surface brightness profiles of red massive galaxies at $0.3 < z < 0.5$. The surface brightness profiles of individual massive galaxies ($\log_{10} M_*/M_\odot > 11.4$) can be measured up to ~ 100 kpc at such intermediate redshifts.

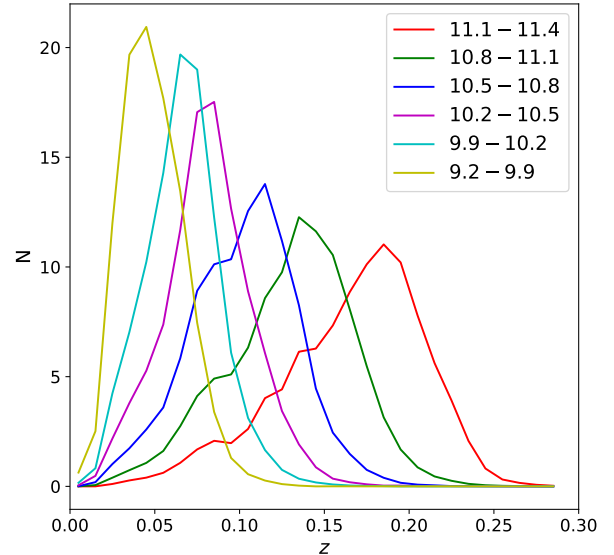


Figure 1. Normalised redshift distributions of isolated central galaxies in six log stellar mass bins ($\log_{10} M_*/M_\odot$). More massive galaxies extend to higher redshifts.

These are the massive brightest cluster galaxy (BCGs) in galaxy clusters.

In this work, we aim to stack the Hyper Suprime-Cam imaging data around a sample of isolated central galaxies that are brighter than all the other local companions at $z \sim 0.1$. Tested against a mock galaxy catalogue based on cosmological simulations, these galaxies are mostly central galaxies of dark matter haloes. They span a wide range of stellar mass, which enables us to push down to smaller stellar mass and larger radial scales by stacking their images.

For observational results, we adopt as our fiducial cosmological model the first-year Planck cosmology (Planck Collaboration et al. 2014), with present values of the Hubble constant $H_0 = 67.3 \text{ km s}^{-1} / \text{Mpc}$, the matter density $\Omega_m = 0.315$ and the cosmological constant $\Omega_\Lambda = 0.685$.

2 DATA

2.1 Isolated central galaxies

To identify a sample of galaxies with a high fraction of central galaxies in dark matter haloes (purity), we select galaxies that are the brightest within given projected and line-of-sight distances. The parent sample used for this selection is the NYU Value Added Galaxy Catalogue (NYU-VAGC; Blanton et al. 2005), which is based on the spectroscopic Main galaxy sample from the seventh data release of the Sloan Digital Sky Survey (SDSS/DR7; Abazajian et al. 2009). Following D’Souza et al. (2014), we at first exclude galaxies whose minor to major axis ratios are smaller than 0.3, which are likely edge-on disc galaxies. de Jong (2008) pointed out that the scattered light through the far wings of

point spread function (PSF) from edge-on disc galaxies can potentially contaminate the stellar haloes.

To select galaxies that are isolated, we require that galaxies are brightest within the projected virial radius, R_{200} , of their host dark matter haloes¹ and within three times the virial velocity along the line-of-sight. Moreover, these galaxies should not be within the projected virial radius (also three times virial velocity along the line-of-sight) of another brighter galaxy. The virial radius and velocity are derived through the abundance matching formula between stellar mass and halo mass of Guo et al. (2010)². The selection criteria have been adopted in Sales et al. (2013), and based on mock catalogues it was demonstrated that the choice of three times virial velocity along the line-of-sight is a safe criterion that identifies all true companion galaxies.

The stellar masses are directly taken from the NYU-VAGC catalogue, which were estimated by fitting stellar population synthesis models to the K-corrected galaxy colour assuming a Chabrier (2003) initial mass function (Blanton & Roweis 2007).

The SDSS spectroscopic sample suffers from the fiber-fiber collision effect that two fibers cannot be placed closer than $55''$. As a result, galaxies in dense regions such as galaxy clusters and groups could miss spectroscopic measurements. To avoid the case when a galaxy has a brighter companion but this companion does not have available redshift and is hence not included in the SDSS spectroscopic sample, we use the SDSS photometric catalogue to make further selections. The photometric catalogue is the value-added Photoz2 catalogue (Cunha et al. 2009) based on SDSS/DR7, which provides photometric redshift probability distributions of SDSS galaxies. We further discard galaxies that have a photometric companion whose redshift information is not available but is within the projected separation of the given selection criterion, and the photoz probability distribution of the photometric companion gives a larger than 10% of probability that it shares the same redshift as the central galaxy, based on the spectroscopic redshift of the central galaxy.

Fig. 1 shows the redshift distribution of selected galaxies in a few different stellar mass bins, indicated by the legend. The distribution spans from $z = 0$ to slightly above $z = 0.25$. Due to the cosmic redshift and time-dilution effect, the observed bands are redder for galaxies at higher redshifts. In principle, to ensure fair comparisons for galaxies at different redshifts, proper K-correction is needed to transfer observed-frame magnitudes and colours to rest-frame quantities. However, K-correction often relies on modelling of galaxy photometry. Model templates for the faint stellar halo in outskirts of galaxies is theoretically not well studied, whereas applying templates of central galaxies to the outer stellar halo might be dangerous, which may potentially introduce additional uncertainties. So instead of involving K-corrections, we choose to use galaxies in a narrow redshift range of $0.05 < z < 0.16$ for our analysis. The amount of K-correction is negligible compared with the difference among

the surface brightness profiles of galaxies in different stellar mass bins.

Huang et al. (2018a) converted the observed surface brightness to stellar mass assuming that the massive galaxies can be well described by an average stellar mass to light ratio. Huang et al. (2018a) achieved SED fitting and K-correction using the five-band HSC cModel magnitudes. In our analysis, we choose to focus on the surface brightness instead of looking at the stellar mass mainly because of the following reasons. First of all, we aim to push to less massive galaxies, which are composed of more complicated stellar populations. The average stellar mass to light ratio cannot be trivially applied to the whole galaxy and the faint stellar halo in outskirts. Secondly, the colour profiles of galaxies are not constants, which vary with radius, and thus using fixed and radius-independent magnitudes for SED fitting would introduce additional uncertainties. We choose to avoid this in our analysis. In principle, we can model the multi-band magnitudes as a function of radius, but we postpone this to our future studies and in this paper we simply focus on the surface brightness. Lastly, as we have mentioned above, model templates for central galaxies might not be directly applicable to the extended stellar halo.

The number of selected galaxies in different mass ranges and within the HSC footprint (the internal S18a data release) is summarised in the second column of Table 1. In the next subsection, we investigate the sample purity, completeness and average halo virial radius, using a mock galaxy sample. We will show the selected sample has a purity of about 85% true halo central galaxies, and hence we call this sample of galaxies as isolated central galaxies.

2.2 Purity and completeness implied from a mock galaxy catalogue

Applying the same selection criteria to simulated galaxies in a mock catalogue, we investigate the sample purity and completeness. The mock galaxy catalogue is based on dark matter halo merger histories from the cosmological Millennium simulation, galaxy formation and evolution are modelled following the physics of Guo et al. (2011). It matches well the observed properties of real galaxies in the local universe, including luminosity, stellar mass distributions and clustering. The Millennium simulation is based on the first-year data of WMAP (Spergel et al. 2003).

To select a sample of isolated central galaxies in analogy to SDSS, we project the $z = 0$ output of the simulation box along z -axis. Each galaxy in the simulation is assigned a redshift based on its z coordinate and its velocity along the z direction. Selections are then made based on the projected separation and redshift difference in the same way as for observational data³. However, it fails to include observational effects such as the flux limit of the real survey, the K-corrections to obtain rest-frame magnitudes, and the incompleteness of close pairs caused by fibre collisions and the complex geometry of SDSS. Using a full light-cone mock catalogue, Wang & White (2012) and Wang et al. (2014) have

¹ R_{200} is defined to be the radius within which the average matter density is 200 times the mean critical density of the universe.

² We have also tested the stellar mass and halo mass relation derived through Halo Occupation Modelling of Wang & Jing (2010), and it gives very similar results in terms of the sample selection.

³ Instead of using the true virial radius in the simulation, we estimate the virial radius from the stellar mass through abundance matching, to be consistent with the observational data.

Table 1. Total number of isolated central galaxies within the S18a footprint, average halo virial radius (R_{200} , based on isolated central galaxies in a mock galaxy catalogue rather than direct abundance matching), image size (number of pixels) and pixel size in unit of kpc for six stellar mass bins considered in our study. We also provide the information for a broader bin of $9.2 < \log_{10} M_*/M_\odot < 10.2$, which is a combination of the two least massive bins above, in order to give better signals for results in Sec. 4.2 and Sec. 4.3.

$\log M_*/M_\odot$	N_{galaxy}	R_{200} [kpc]	image size [pixel×pixel]	pixel size [kpc]
11.1-11.4	1438	459.08	1500×1500	1.83
10.8-11.1	5068	288.16	1000×1000	1.72
10.5-10.8	5572	214.80	750×750	1.71
10.2-10.5	3331	173.18	600×600	1.73
9.9-10.2	1536	142.85	500×500	1.71
9.2-9.9	801	114.64	400×400	1.72
9.2-10.2	2337	120.76	400×400	1.81

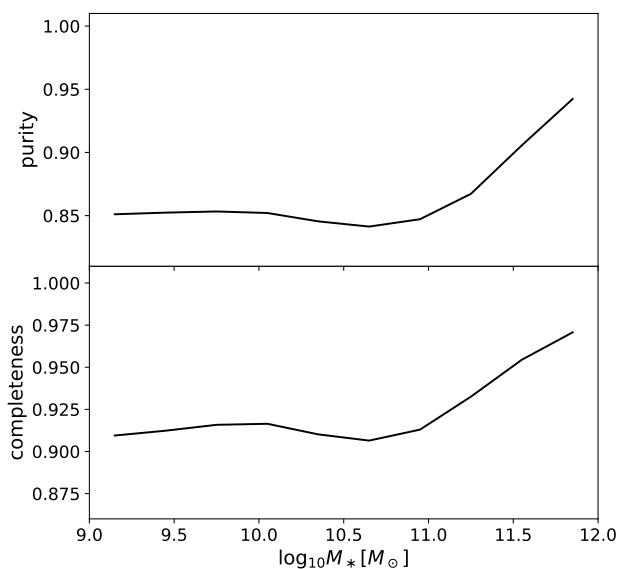


Figure 2. The purity of true halo central galaxies of isolated central galaxies (upper panel), and the completeness of isolated central galaxies with respect to all central galaxies (lower panel), reported as a function of stellar mass. The purity and completeness are based on a mock galaxy catalogue.

compared satellite properties based on such direct projections and found that the direct projection gives unbiased results.

The purity and completeness are shown in Fig. 2. The purity is above 95% at the massive end, and drops to almost a constant fraction of about 85% at $9.2 < \log_{10} M_*/M_\odot < 11$. The completeness fraction is about 96% at the massive end, and drops to slightly above 90% at $9.2 < \log_{10} M_*/M_\odot < 11.2$.

In a few previous studies which probe the gas content of galaxies through Sunyaev-Zeldovich effect (Planck Collaboration et al. 2013, 2016; Hernández-Monteagudo et al. 2015), X-ray (Anderson et al. 2015), calibration of the scaling relations between SZ signal/X-ray luminosity and halo mass through weak gravitational lensing (Mandelbaum et al.

2016; Wang et al. 2016), we select galaxies which are brightest within a projected separation of 1 Mpc and within 1000 km/s along the line-of-sight. 1 Mpc is larger than the mean halo virial radius at $\log_{10} M_*/M_\odot < 11.5$, and 1000 km/s is comparable to three times the mean virial velocity for galaxies with $\log_{10} M_*/M_\odot \sim 11.1$. Thus for galaxies smaller than $\log_{10} M_*/M_\odot = 11.1$, the 1 Mpc (1000 km/s) selection is more rigorous than the selection criteria introduced earlier in this section.

For the purpose of this study, we need to balance between a large enough sample size in order to obtain good signals and a high enough fraction of true halo central galaxies to avoid possible contamination from nearby massive galaxies. So we focus on our current sample. The less stringent selection gives a larger sample size, which helps us to push to smaller stellar mass ranges and larger radial scales of the surface brightness profiles. In Appendix C, we make comparisons to the sample of galaxies selected by the 1 Mpc criteria in those previous studies, to show the robustness of our results to the sample selection and to the purity of central galaxies.

The third column from the left of Table 1 provides the average virial radius, R_{200} , for isolated central galaxies in different stellar mass ranges of the mock catalogue. The average R_{200} of isolated central galaxies can be biased from that of all central galaxies in the corresponding stellar mass bin. Thus, although we have used the virial radius estimated from abundance matching to select our sample of isolated central galaxies, we will use the R_{200} values in Table 1 to determine the corresponding size of image cutouts. Details are provided in Sec. 3.

2.3 HSC photometry and data reduction

The Hyper Suprime-Cam Subaru Strategic Program Survey (Aihara et al. 2018, hereafter HSC-SSP or HSC;) is based on the new prime-focus camera, the Hyper Suprime-Cam (Miyazaki et al. 2012, 2018; Komiyama et al. 2018; Furusawa et al. 2018) on the 8.2-m Subaru telescope. It is a three-layer survey, aiming for a wide field of 1400 deg^2 with a depth of $r \sim 26$, a deep field of 26 deg^2 with a depth of $r \sim 27$ and an ultra-deep field of 3.5 deg^2 with one magnitude fainter. It involves five bands, i.e., HSC-*grizy*. The transmission range of wavelengths for each of the HSC *gri*-bands is almost the same as that of SDSS (Kawanomoto et al. 2018).

HSC-SSP data is processed using the HSC pipeline. The pipeline is an enhanced version of the LSST (Large Synoptic Survey Telescope; [Axelrod et al. 2010](#); [Jurić et al. 2015](#)) pipeline code, specialised for HSC. Details about the HSC pipeline are available in the pipeline paper ([Bosch et al. 2018](#)), and here we only introduce the main data reduction steps and corresponding data products of HSC.

HSC has 104 main science CCDs, which are arranged on the focal plane and provide a 1.5 deg field of view in diameter. Gaps exist between CCDs, and there are two different gap size ([Komiyama et al. 2018](#)), approximately 12" and 53" between neighbouring CCDs. In the context of HSC, a single exposure is called one "visit" with a unique "visit" number. The same sky field is observed or "visited" multiple times, and hence for the same object, it can appear for multiple times on different CCDs (or different locations of the focal plane). The HSC pipeline involves four main steps: (1) processing of single exposure/visit image (2) joint astrometric and photometric calibration (3) image coaddition and (4) coadd measurement.

In the first step, bias, flat field and dark flow are corrected for. Bad pixels are masked and interpolated. The sky background is estimated and subtracted for source detections (see Sec. 2.4 for more details about the background subtraction). Detected sources are matched to external reference catalogues in order to calibrate the zero point and a gnomonic world coordinate system (TAN-SIP) for each CCD. After galaxies and blended objects are filtered out, a secure sample of stars are used to construct the PSF model. The background-subtracted images and the subtracted background models are both stored to the disc. The output products of this step are called Calexp images. They are given on individual exposure basis.

In HSC, four lamps in the dome are used for the flat field. Flat fielding with the dome flats is a necessary and crucial step which helps to flatten the sky and aids to fit and remove the sky background. However, the effective temperature are not the same for different lamps, and the camera vignetting ([Miyazaki et al. 2018](#)), which is a reduction of the brightness or saturation for the periphery of images compared to the image center, also couples individual lamps to particular areas on the focal plane, which prevent the flat field from being ideally flat. In addition, the pixel size of CCDs varies ([Miyazaki et al. 2018](#)). Pixels near the edge of the CCD plate can be about 10% smaller in area than pixels sits at the center of the plate. Since pixel values in both data images and the flat fields are flux instead of surface brightness or intensity (not divided by the pixel size), after detrending the flat field, pixel area variations over the CCD plate are interpreted as quantum efficiency and divided out. However, as we will describe in the third coaddition step, the relative area variation between input and output pixels is still considered for resampling before coaddition. To correct for the non-uniform flat field and put back pixel size variations, a mosaic correction step is run by including the Jacobian matrix that reflects pixel area variations, modelling and correcting for the flux across images using a seventh order polynomial, in order to make the measured flux of sources consistent with that of the reference stars. This improves both astrometry and photometry.

In the second joint calibration step, the astrometric and photometric calibrations are refined by requiring that the

same source appearing on different locations of the focal plane during different visits should give consistent positions and fluxes. Readers can find details in [Bosch et al. \(2018\)](#). The joint calibration step improves the accuracy of both astrometry and photometry. The difference for the same sources on different CCDs peaks at 35 mas without the joint calibration step, while it decreases to 10 mas after joint calibration.

In the third step, the HSC pipeline resamples images to the pre-defined output skymap (warping) by properly considering the relative area variations and the overlapping fraction for pixels between inputs and outputs. It involves resampling of both the single exposure images and the PSF model ([Jee & Tyson 2011](#)) to the common output skymap using a 3rd-order Lanczos kernel (e.g. [Turkowsky 1990](#)). All warped/resampled images are combined together (coaddition). The inverse of the average values of the variance in each image are used as weights for coaddition. Compared with direct averages or single long-time exposures, the weighted average gives better signal-to-noise and also helps to avoid pixel saturation. Images produced through warping and coaddition are called coadd images.

In the last step, objects are detected, deblended and measured from the coadd images. For our analysis in this paper, we focus on image-level analysis without referring to the HSC source catalogue, so this last step is not directly related to our science. We refer the readers to the pipeline paper for more details ([Bosch et al. 2018](#)).

2.4 Improved background subtraction

The faint stellar halo can be less than a few percent level of the mean sky background, and thus it is very important to properly model and subtract the background, which is a challenging task. One complication comes from the fact that the true sky background is often mixed with other factors such as the scattered light from bright objects and instrumental features. For example, the filter response curve shows strong radial dependence ([Kawanomoto et al. 2018](#)) in both HSC-*r* and HSC-*i* filters⁴, which brings in ring-like structures crossing all CCDs⁵ (see Fig. 3). These features are mixed with the true sky background.

The HSC internal data releases S15, S16 and S17 use a 6th-order Chebyshev polynomial to fit individual CCD images to model the background. It over-subtracts the light around bright sources and leaves a dark ring structure around bright galaxies. The over-subtraction is mainly caused by the scale of the background model (or order of the polynomial fitting) and unmasked outskirts of bright objects. It is difficult to know how extended objects are before coaddition. The new version of HSC pipeline (v6.5.3) and the latest internal data release (S18a) implement a significantly improved background subtraction approach (HSC

⁴ New filters of HSC-*r*2 and HSC-*i*2 have been procured ([Kawanomoto et al. 2018](#)), which do not have these features.

⁵ In Fig. 3, we show the stack based on S15b Calexp images, because S18a Calexp images were not released upon writing up the paper, but the pattern of instrumental features should be very similar for background-unsubtracted raw images of S15b and S18a.

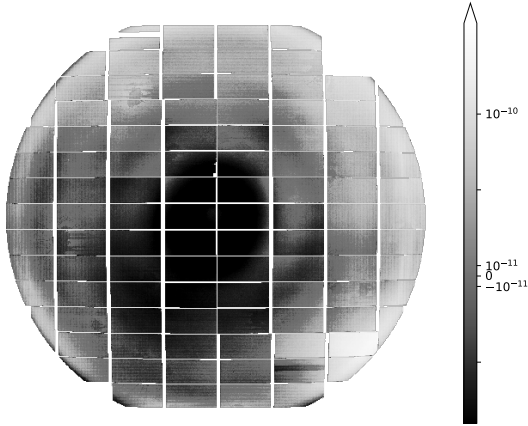


Figure 3. Stack of all visits (Calex images) in HSC-*r* filter of the S15b internal data release. The subtracted background model has been added back, after which a mean background is estimated and subtracted for each plate before stacking, and hence there are negative pixel values. Pixel values are intensity, I , divided by zero point intensity, I_0 . Note $-2.5 \log_{10} I/I_0$ gives the surface brightness in unit of magnitudes. To show negative values, regions of $I/I_0 > 10^{-11}$ and $I/I_0 < -10^{-11}$ are displayed in log scales for the absolute values, while the region of $-10^{-11} < I/I_0 < 10^{-11}$ is in linear scale. Sources are masked before stacking. Incomplete masking of very extended bright stars leaves a few small hole and spike like features. The large scale and ring-like structures are due to the radial-dependence of the filter response.

Collaboration et al., 2019, in preparation). It jointly models the sky background and instrumental features using all CCDs, meaning that discontinuities at CCD edges are avoided. The ring-like structures crossing different CCDs as shown in Fig. 3 are modelled and removed. In addition, a larger scale of about 1000 pixels is adopted to model the background, which minimises over-fitting due to small scale fluctuations.

In our analysis throughout the main text of this paper, we focus on results based on the coadd images of the S18a release, with background subtracted by the pipeline. We introduce our methodology of processing these coadd images of S18a in the next section. In Appendix A, we show a comparison between results based on S15b and S18a coadd images, to demonstrate the significant improvement of background subtraction in the latest S18a release. In Appendix B, we also provide results based on our own reprocessed Calex images in the S15b release, to further test and validate the robustness of background subtraction for S18a. In the test we add the subtracted background model back and apply our own statistical background subtraction approach.

3 METHODOLOGY

In the following, we describe the steps of processing S18a coadd images.

3.1 Image cutouts and zero point correction of flux

Given the celestial coordinates of our galaxy sample and the average virial radius, R_{200} , in different mass bins, we extract image cutouts, which are approximately square sky regions centered on each galaxy with a side length of $6R_{200}$. The physical R_{200} is transformed to angular scales at the redshift of the galaxy. Pixel values of each image is divided by the zero point flux, which is produced by the pipeline with reference stars (see Sec. 2.3).

3.2 Image resampling

The pixel size of HSC images has a fixed angular size of about $0.17''$, and hence the number of pixels within a given physical scale can vary significantly for galaxies at different redshifts. To stack images in physical coordinates, we need to resample the image cutouts to a common grid of pixels with the same physical size. This is achieved by the warping module of HSC pipeline. It “warps” input images to a pre-defined output WCS, image size and pixel size. Basically, for a given output pixel and its central coordinate, the module at first resamples the input pixels at the location of the output pixel. The procedure is accomplished through Lanczos sampling, i.e., the pixel value at position x is given by the convolution between discrete pixel values and the third order Lanczos function. The Lanczos function serves as a filter to reconstruct pixel values at any given position, according to the Nyquist sampling theorem. The resampled value is then corrected for the change in the pixel area from the input to the output image.

After resampling, the number of pixels is exactly the same for all images centered on galaxies in the same stellar mass bin, and these resampled images will be stacked afterwards. Each pixel corresponds to a given physical scale instead of angular scale. The image size (number of pixels) and pixel size (in unit of kpc) are provided in the fourth and fifth columns of Table 1. We have carefully tested that changing the image and pixel size within a reasonable range does not affect the final stacked surface brightness or colour profiles of the stellar halo.

3.3 Cosmic dimming correction

The pixel values are in unit of flux, and we divide them by the corresponding pixel area (solid angle), which gives the surface brightness or intensity in each pixel. The surface brightness is a conserved quantity that does not vary with the distance in Euclid space, but in the expanding universe it scales with redshift, z , in the manner of $(1+z)^{-4}$, which is called “cosmic dimming”⁶. To correct for the effect,

⁶ Strictly speaking, the scaling with redshift of cosmic dimming is perfectly valid for bolometric luminosity or a fixed band. For an identical object at different redshifts, we are observing different

each image is multiplied by $(1+z)^4/1.1^4$, i.e., correcting the intensity to $z = 0.1$.

3.4 Source masking

Bad pixels such as those which are saturated, close to the edge, outside the footprint with available data, hit by cosmic rays and so on, are masked by the pipeline. Moreover, to investigate the smooth stellar halo of the central galaxy, we need to mask all the companion sources and the extended light emissions of companions. To create deep masks, we at first resample and stack all coadd images in HSC g , r and i -bands. We then run SExtractor on these images, using a detection threshold of 0.8 times the background fluctuation. SExtractor outputs “segments” of detected sources. The segments can be used to mask out an extended region of pixels associated with companion sources such as stars, satellite galaxies and projected foreground/background objects. The low detection threshold helps to mask an extended region centered on sources, which safely removes their extended emissions.

However, it also results in many fake detections which are in principle background noise. Removing pixels associated with these fake detections may potentially modify the background fluctuation or noise level, and may probably decrease the signal-to-noise ratio. To test whether a low detection threshold can affect our results, we provide tests in Appendix D that adopting a higher detection threshold makes the measured surface brightness profiles drop a bit more quickly beyond a few tenth of kpc scales, which reduces the largest projected scale that we can reach. These are likely caused by the extended emission of companion sources that are not fully masked. Despite the small difference, the higher detection threshold produces consistent results.

3.5 Clipping and stacking

We stack all images in a weighted average manner. For each image in the HSC database, a corresponding variance map (Poisson error) is also provided. Upon warping input images to the output plane, the variance map is also projected to the output plane through error propagation⁷. After masking pixels associated with all detected companion sources by SExtractor, we use the inverse of the $2\text{-}\sigma$ clipped mean values of these variance maps as weights for stacking. We have carefully checked that weighted and unweighted average of input images give very similar results that are consistent with each other, but the former has slightly smaller errors in the final stacked image.

As mentioned above, pixels associated with companion sources are masked out. Besides, for regions that do not contain available data, such as CCD gaps and edges, the

bands. Proper K-correction is necessary for fair comparison of objects at different redshifts and for proper “cosmic dimming” corrections. But as we have discussed in Sec. 2.1, K-corrections of the outer stellar halo might introduce additional uncertainties, and we choose to focus on a narrow redshift range to avoid K-corrections.

⁷ The output variance map is not perfectly accurate, because errors are correlated across pixels, but we choose to ignore the imperfection in our analysis.

pixels are treated as NaN values and masked as well. As a result, the true number of pixels contributing to the final stack varies over the output image by about 30% to 40% from the center to the periphery of image cutouts. For each pixel in the output, we also clip the sample of all useful input pixels by discarding 10% brightest and faintest pixels. We have checked that varying this fraction between 1% and 10% does not bias the stacked light and colour profile, but it helps to smooth the final stacked image.

In the end, we note that some previous studies (e.g. D’Souza et al. 2014; Huang et al. 2018a) derived surface brightness profiles using isophotal ellipses centered on galaxies. In this study, we will not rotate or align galaxies, and hence the surface brightness profiles derived in this study are simply circularly averaged profiles.

3.6 Random sample correction for residual background

The sky background and instrumental features have already been modelled and subtracted off by the pipeline for coadd images, but there might be residual background remained to a certain level, which can be either positive or negative. The amount of the residual background is very small, which is only a few percent level of the true night sky background, but it is comparable to the stellar halo emission in outskirts of galaxies and hence has to be corrected. Correcting for such a residual background is very important for us to study the faint stellar halo light on large scales. To achieve the correction, we repeated the same steps for a sample of random points, whose sky coordinates are randomly distributed within the survey footprint. The random sample size is chosen to be comparable with that of real galaxies. In addition, we force the random sample to have exactly the same stellar mass and redshift distributions as that of real galaxies, to ensure the same angular size distributions for images. Note for each individual image, its edge length is the angular scale that corresponds to $2 \times 3R_{200}$ (see Table 1) at the redshift of the central object. The stacked image or surface brightness profiles centered on these random points are used as an estimate of the residual background, and are further subtracted from the stacks centered on real galaxies. This residual background also accounts for the average cosmic background to be subtracted from the stacked stellar profiles.

4 RESULTS

4.1 surface brightness and colour profiles split by stellar mass

The stacked images of galaxies in RGB colour are presented in Fig. 4, for six stellar mass bins of Table 1. In addition, We also provide three stacked images centered on random points, which have exactly the same redshift and image size distributions as real galaxies in three out of the six stellar mass bins (see text on top). We choose not to show all random stacks to simplify and shorten the figure. The RGB images are based on the stacked images in HSC g , r and i -bands, and mapped to the RGB colour following the colour mapping strategy of Lupton et al. (2004).

From the most massive population of galaxies in the

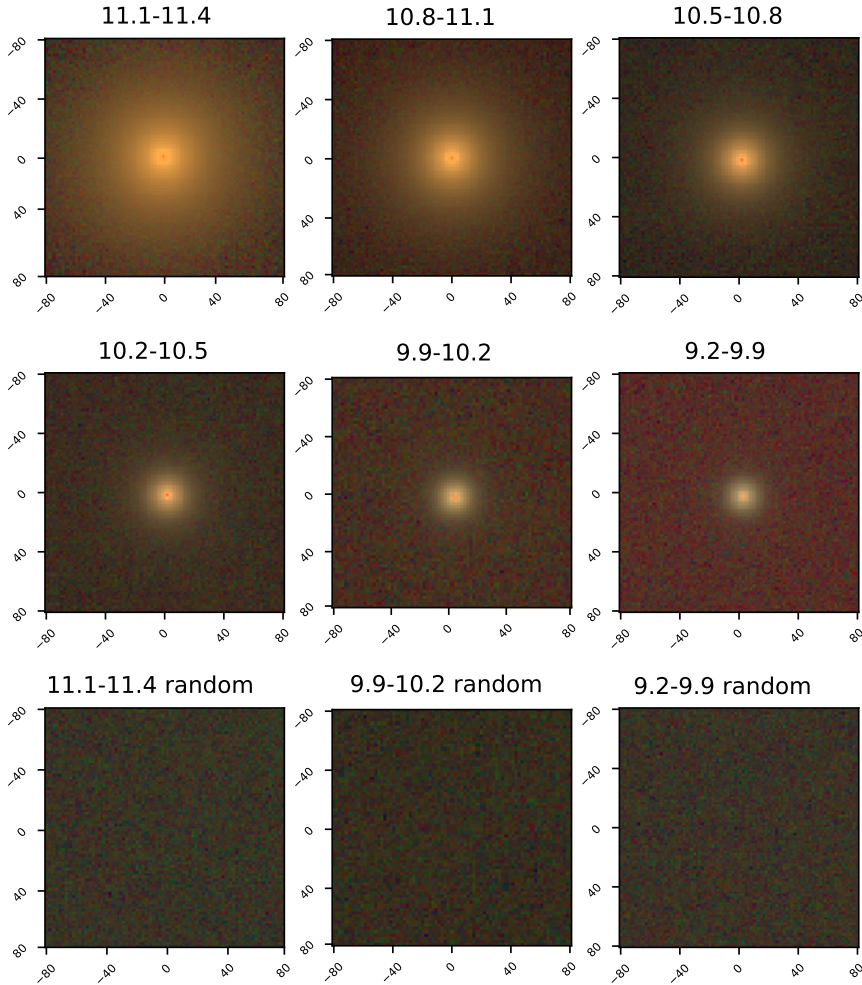


Figure 4. From top left to middle right are stacked and residual background corrected images of galaxies in RGB colour, obtained through images in HSC g , r and i -bands. The stellar mass range of galaxies used for stacking in each panel is indicated by the text on top. The three images in the bottom are stacked images based on random points that share the same assigned redshift and image size distributions as real galaxies in the most massive and the two least massive bins (see the text on top). The colour scales of all six panels are exactly the same. Image edge lengths are 160 kpc, i.e., ranging from -80 kpc to 80 kpc.

top left to the least massive galaxies in the middle right, the galaxy size decreases, and the surface brightness on a given radius to image center decreases as well. The colour transition is also obvious that more massive galaxies are redder. It is very encouraging that the stacked images centered on random points are smooth and uniform, which proves that our image processing is successful.

Binned in projected radial distance to the galaxy center, r_p , the one-dimensional surface brightness profiles in HSC r -band are presented in Fig. 5. We show both the Poisson errors and boot-strap errors. For the latter, we generate 100 boot-strap samples by randomly selecting galaxies from the original sample with repeats. Each boot-strap sample has exactly the same sample size as the original sample, and the standard deviation of the 100 samples give the boot-strap error. The reader can also find the one-dimensional surface brightness profile centered on a random sample in Appendix A. It is shown that the one-dimensional profile

stacked on random points is ideally flat, and on large scales it agrees very well with the profile stacked on real galaxies.

It is very encouraging to see that, though the survey footprint of HSC is much smaller than SDSS, we can measure the surface brightness profiles out to about 120 kpc, with indications of further signals even beyond. We can still have positive measurements at 200 kpc and even larger scales, though on such scales the errors are very large, with the lower error boundaries going negative. The faintest surface brightness that we can reach is 29.5 mag/arcsec² for the most massive bin at 120 kpc. For galaxies with $9.2 < \log_{10} M_*/M_\odot < 11.1$, we can push to about 31 mag/arcsec² to slightly brighter than 33 mag/arcsec² at 120 kpc.

Stacking SDSS images, D’Souza et al. (2014) measured the surface brightness profiles in r -band out to slightly beyond 100 kpc for galaxies in the mass range $10 < \log_{10} M_*/M_\odot < 11.4$. The depth that they can achieve is about 32 mag/arcsec². Despite the fact that the total sky

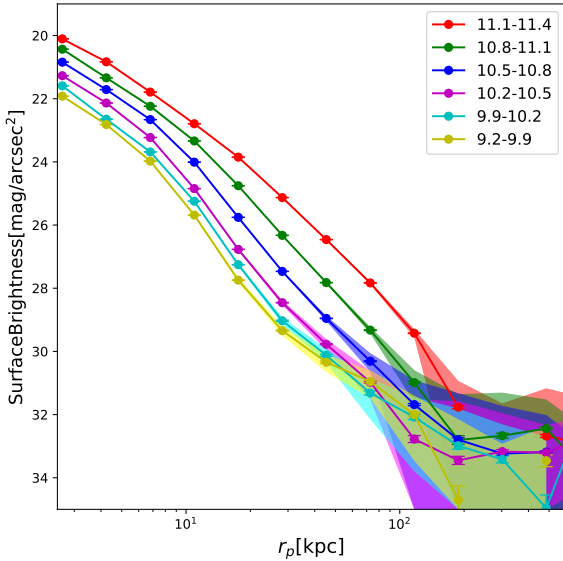


Figure 5. Average surface brightness profiles in HSC r -band and centered on galaxies in six stellar mass bins, as indicated by the legend. Short errorbars are Poisson errors. Within 80 kpc, the Poisson errors are mostly comparable to the symbol size. Shaded regions show the $1\text{-}\sigma$ scatter of the stacked profiles based on 100 boot-strap resampled realisations.

footprint of the S18a internal release of HSC is at least twenty times smaller⁸ than SDSS/DR7, the significantly deeper HSC survey with high image qualities has enabled us to push to larger scales, fainter surface brightness and smaller galaxies, which is very encouraging.

The measured surface brightness profiles are true light distributions convolved with the PSF. On scales smaller than and comparable to the typical Full Width at Half Maximum (FWHM) size of the PSF, the inner regions of PSF convolved profiles are systematically flattened compared with the true profiles. The HSC data product provides PSF information, measured on bright stars and interpolated over the whole image. We output the PSF size at the centre of each galaxy, and convert the PSF in unit of arcsecond to the physical separation at the redshift of the galaxy. The average FWHM from the most to least massive bins are $0.756''$, $0.759''$, $0.752''$, $0.755''$, $0.7508''$ and $0.7501''$. The corresponding mean physical separations are 1.759 kpc, 1.693 kpc, 1.483 kpc, 1.278 kpc, 1.126 kpc and 0.984 kpc, respectively. Note the redshift distribution for less massive galaxies are on average lower, so a given angular scale corresponds to a smaller physical scale. The typical physical scale of the PSF size is smaller than the inner most point presented in Fig. 5, and hence we expect our results are not significantly affected by the PSF. So we choose not to include PSF deconvolution in our results, but in Sec. 4.3 and

⁸ Our isolated central galaxies are selected from the VAGC catalogue of SDSS/DR7, and about one-third of the S18a footprint does not overlap with SDSS/DR7. Hence the effective area can be even smaller.

Sec. 5, we will fit theoretical models to the measured surface brightness profiles, and we will convolve the theoretical profiles with the typical (weighted average) PSF in each bin.

The difference between surface brightness profiles measured in different filters give the colour profiles. Note the PSF size can vary for different filters, but as we have discussed above, the typical PSF size is smaller than the inner most data point in our measurements, and hence our colour profiles are unlikely to be significantly affected by the PSF size difference crossing HSC g , r and i -bands. The colour profiles are shown in Fig. 6. Throughout the paper, the Poisson errors are all smaller than the boot-strap errors⁹, and hence from now on we choose to show only the boot-strap errors.

We can measure $g - r$ and $g - i$ colour profiles out to about 100 kpc. Two general trends are clearly revealed from Fig. 6. Firstly, we see massive galaxies are redder, which is in good agreement with Fig. 4. Moreover, for galaxies in a fixed stellar mass range, the colour is redder in the inner region and bluer outside. However, in the left plot, the few outer points for galaxies with $9.2 < \log_{10} M_*/M_\odot < 10.5$ tend to show positive gradients in their $g - r$ colour. In the right plot, galaxies with $9.2 < \log_{10} M_*/M_\odot < 9.9$ also show very significant positive gradients in their $g - i$ colour. The positive gradients or redder colour in outskirts of galaxies between 30 kpc and 80 kpc can also be seen in the two least massive panels of Fig. 4, that the outskirts of the panels are surrounded by noisy colour spots, but the colours are on average redder than the outskirts of other panels. On such scales, the associated uncertainty levels as shown by the size of errorbars in Fig. 6 are also very large.

D’Souza et al. (2014) investigated the colour profiles around isolated central galaxies at $0.06 < z < 0.1$. Their results also show reddest colour in the very central regions of galaxies and bluer colours at about 10 kpc, and they detected redder colours in outer regions. However, the stellar mass and scale ranges for such positive gradients in their measured $g - r$ colour profiles are different from ours. In their results, the colour profiles of galaxies with $10 < \log_{10} M_*/M_\odot < 11.4$ show flattened or positive gradients beyond scales of about 10 to 20 kpc.

D’Souza et al. (2014) divided their sample of galaxies into two subsamples of low and high concentration galaxies, and they reported distinct features in the colour gradients of low and high concentration galaxies. In the next subsection, we split our sample of galaxies into low and high concentrations and further investigate their surface brightness and colour profiles.

4.2 surface brightness and colour profiles split by galaxy concentration and stellar mass

Following D’Souza et al. (2014), we investigate the surface brightness and colour profiles for galaxies split into two subsamples with high concentrations ($C > 2.6$) and low concen-

⁹ The Poisson error map for each individual image is propagated to the final stacked image in the same weighted average manner as for real images, but the scatter among different images, which is reflected by the boot-strap errors, are not included in the Poisson errors.

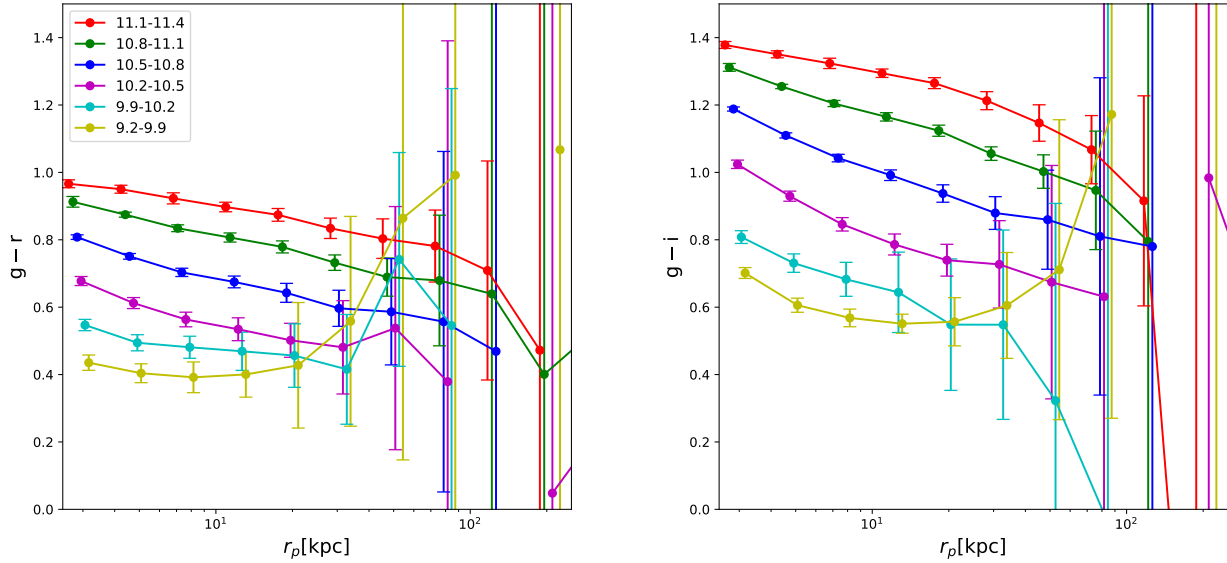


Figure 6. $g - r$ (left) and $g - i$ (right) colour profiles. Errorbars are $1-\sigma$ errors obtained from 100 boot-strap resampled realisations. Small shifts have been added to x for the second to the least massive bins, to better display the errorbars.

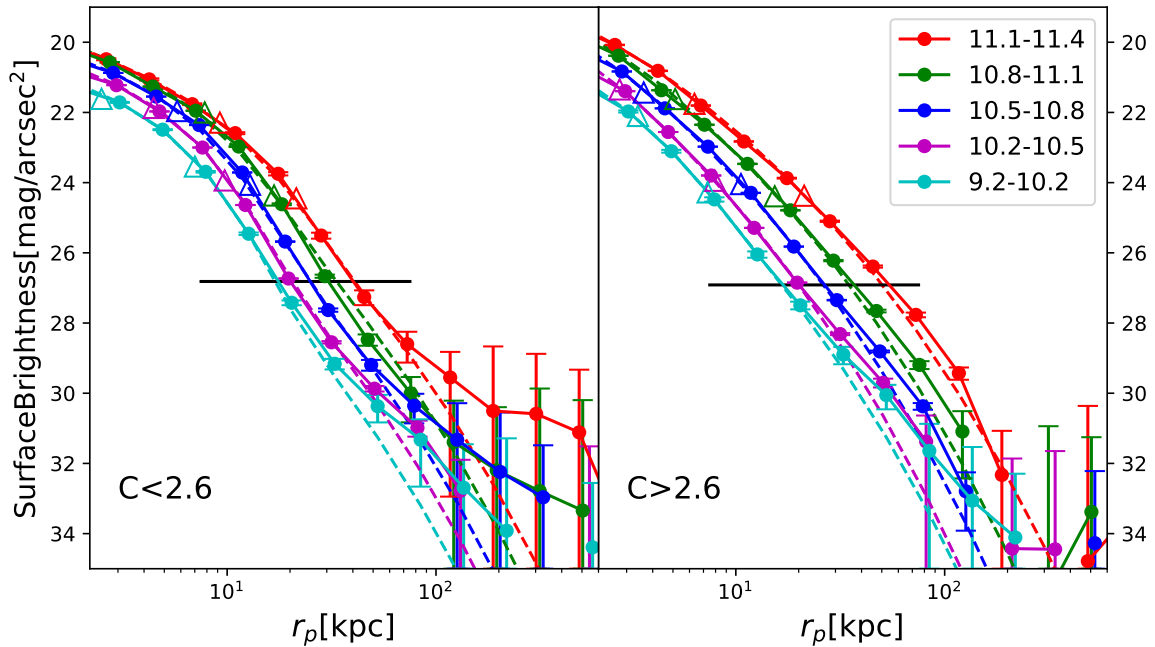


Figure 7. **Left:** Surface brightness profiles (dots connected by solid lines) in HSC r -band for galaxies with concentration, C , smaller than 2.6, and in five stellar mass bins as indicated by the legend. **Right:** Similar to the left panel, but shows surface brightness profiles for galaxies with concentration larger than 2.6. Errorbars in both panels are the $1-\sigma$ scatter of 100 boot-strap realisations. The black horizontal lines mark the average rms of the background noise for single images before stacking. Dashed lines of the corresponding colour are cModel fits (PSF convolved) to the measurements above the background noise level. The two empty triangles with corresponding colour and associated with each curve show the mean radii that contain 90% and 50% of the Petrosian flux for galaxies in each bin. Small shifts have been added to x for the second to the least massive bins.

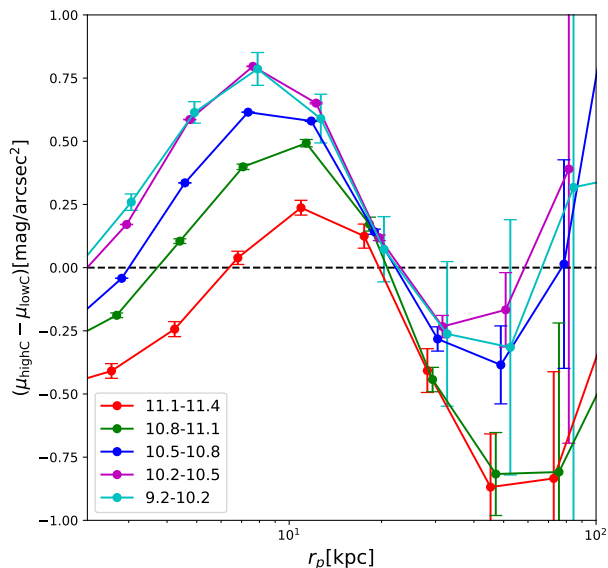


Figure 8. The surface brightness profiles of high concentration galaxies minus the surface brightness profiles of low concentration galaxies in HSC r -band. Negative and positive values mean the profiles of high concentration galaxies are brighter and fainter, respectively. Small shifts have been added to the second to the least massive bins along x -axis.

Table 2. Number of low ($C < 2.6$) and high ($C > 2.6$) concentration galaxies

$\log M_*/M_\odot$	$C < 2.6$	$C > 2.6$
11.1-11.4	169	1269
10.8-11.1	1416	3652
10.5-10.8	2638	2934
10.2-10.5	2223	1108
9.2-10.2	1994	343

trations ($C < 2.6$). Here the galaxy concentration is defined as the ratio of the radii that contain 90% and 50% of the Petrosian flux in r -band¹⁰, i.e., $C = R_{90}/R_{50}$. We choose the cut at $C = 2.6$ to be consistent with D’Souza et al. (2014). The number of low and high concentration galaxies in different stellar mass bins are provided in Table 2.

After dividing galaxies into subsamples of high and low concentrations, it is difficult to maintain enough signal-to-noise ratios for the two least massive bins ($9.9 < \log_{10} M_*/M_\odot < 10.2$ and $9.2 < \log_{10} M_*/M_\odot < 9.9$), es-

¹⁰ The radii that contain 90% and 50% of the Petrosian flux are downloaded from the SDSS database. Deep HSC images can potentially improve the measured Petrosian radius and flux, but we just focus on measurements from SDSS for our isolated central galaxies. This is because we want to make more fair comparisons with D’Souza et al. (2014), and the SDSS spectroscopic sample is bright enough to ensure robust measurements, which already satisfies our science purposes.

pecially for high concentration galaxies because low mass galaxies are less concentrated. Hence we choose to merge the two least massive bins into a single stellar mass bin (the bottom row of Table 1). The surface brightness and colour profiles are shown in Fig 7 and Fig. 9, respectively. Left and right panels are for low and high concentration galaxies, and for each, they are further separated into stellar mass bins.

Low and high concentration galaxies show clear differences in their surface brightness profiles. Less concentrated galaxies in the left panel of Fig 7 are more extended beyond 100 kpc. Despite the large errors, the surface brightness profiles extend up to about 500, 500, 300, 120 and 120 kpc for the five stellar mass bins, which are close to or even beyond the halo virial radius (see Table 1). Moreover, the profiles of low concentration galaxies are more flattened in the very central region as a result of the definition of being less concentrated, but then drop faster on scales of $20 \text{ kpc} < r_p < 100 \text{ kpc}$. This is more clearly revealed in Fig. 8 that within 20 kpc, the surface brightness differences between high and low concentration galaxies are mostly positive, which means low concentration galaxies are brighter on such scales. For scales between 20 kpc and 100 kpc, the differences are dominated by negative values, showing high concentration galaxies are brighter. This agrees with the conclusion of D’Souza et al. (2014) that the stellar halo of low concentration galaxies have steeper slopes beyond $r_p = 25 \text{ kpc}$.

To guide the eye, we plot on top of each curve as empty triangles the mean Petrosian radii that contain 90% and 50% of the Petrosian flux (R_{90} and R_{50}). R_{50} of high concentration galaxies are clearly smaller. The black horizontal lines in both panels mark the mean background noise level of individual images before stacking, and triangles are all above the noise level for individual images, which is reasonable because both R_{50} and R_{90} are measured based on individual galaxy images. Dashed lines are fits to data points above the background noise level using a composite model which combines Exponential and de Vaucouleurs model profiles (cModel). We postpone discussions about the fits to Sec. 5.

Our colour profiles for low and high concentration galaxies, however, still disagree with D’Souza et al. (2014) in terms of the positive colour gradients. D’Souza et al. (2014) detected flattened colour profiles for high concentration galaxies, whereas for low concentration galaxies, their measured colour profiles are reddest in the very central parts of galaxies, and become bluer up to some typical radius between 10 kpc and 20 kpc. Beyond the typical radius, their colour profiles tend to show positive gradients and turn redder again.

In Fig. 9, we do see differences in the $g-r$ colour profiles for low and high concentration galaxies. High concentration galaxies have redder colours and shallower negative gradients. However, there is no indications of positive gradients on 10 to 20 kpc scales for the four most massive bins. For the least massive bin (cyan dots and lines) in the left panel, the profile starts to be flattened beyond 10 kpc. In addition, the second least massive bin in the left also shows some bump-like features on 50 to 60 kpc scales. The third bin in the right panel (blue dots and line) has its last point turns up to a significantly red value. The two least massive bins in the right panel also show some bump-like features. However, we need to be careful given the large errorbars on these scales. If the signals of positive gradients are real, the corresponding stel-

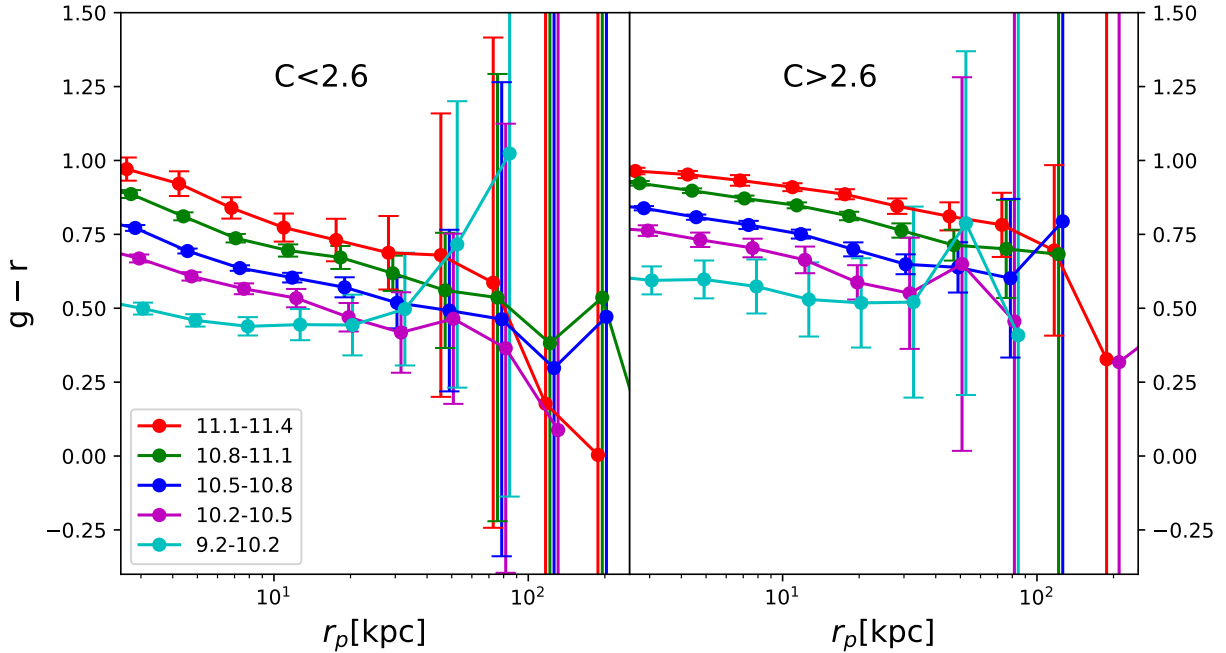


Figure 9. **Left:** $g - r$ colour profiles for galaxies with concentration, C , smaller than 2.6, and in five stellar mass bins as indicated by the legend. **Right:** Similar to the left panel, but shows $g - r$ colour profiles for galaxies with concentration larger than 2.6. Errorbars in both panels are the $1-\sigma$ scatter of 100 boot-strap realisations. Small shifts have been added to x for the second to the least massive bins.

lar mass and scale ranges are not the same as those found by D’Souza et al. (2014). In fact, we will show in Appendix C that with a more strictly selected sample of isolated central galaxies, the bump-like structure in the second to least massive bin ($10.2 < \log_{10} M_*/M_\odot < 10.5$) disappears, so the bump is likely related to satellite contaminations in the sample selection or may simply be statistical fluctuations. But by tuning the isolation criteria, the positive gradient does not go away for galaxies with $9.2 < \log_{10} M_*/M_\odot < 10.2$.

The positive colour gradient in the least massive bin and the disagreement with D’Souza et al. (2014) is puzzling. Given the large errorbars, the measured colour profiles for galaxies with $9.2 < \log_{10} M_*/M_\odot < 10.2$ could be consistent with being flat, especially on scales between 10 kpc and 30 kpc. The reader can find detailed discussions about possible systematics that might contribute to the positive gradients in Sec. 5.2. We also discuss in Appendix C that the disagreement with D’Souza et al. (2014) is unlikely due to the difference in the isolation criteria adopted to select our sample of galaxies.

4.3 Universality of stellar haloes

The density profiles of dark matter haloes, their mass accretion histories, the spatial, mass and phase-space distributions of their accreted subhaloes and satellite galaxies can all be described by unified models once they are scaled by some characteristic quantities (e.g. Navarro et al. 1996, 1997; Zhao et al. 2003, 2009; Han et al. 2016; Li et al. 2017; Callingham et al. 2018). In this section, we investigate whether the surface brightness profiles of the stellar halo can be uni-

fied as well. We look into this in Fig. 10, where the surface brightness profiles of low and high concentration galaxies in different stellar mass ranges are plotted as a function of the projected distance r_p scaled by the halo virial radius R_{200} .

Note, although we estimate R_{200} based on abundance matching to select our sample of isolated central galaxies, the halo mass versus stellar mass relation of selected galaxies can be biased from that of all central galaxies, and thus we highlight again that R_{200} values of isolated central galaxies in Table 1, which are used throughout the paper for determining image and pixel size, and will be used to scale profiles in this section, are all obtained based on isolated central galaxies selected in the mock galaxy catalogue of Guo et al. (2011). Hence R_{200} values in Table 1 are slightly different from those estimated from abundance matching. However, we should bear in mind the uncertainty of R_{200} , which can be quantified by comparing the mock catalogue and true weak lensing measurements. We move on with this uncertainty, and postpone more accurate analysis of R_{200} through weak lensing to future studies.

It is very encouraging that after plotting the profiles as a function of r_p/R_{200} instead of r_p , the amplitudes and shapes of profiles for galaxies with different stellar masses tend to be very similar to each other. Profiles of the most massive bin still differ from the others after the scaling, and for the least massive bin of low concentration galaxies, there are some discrepancies, but for the other stellar mass bins, the profiles are very similar to each other.

We fit the following double Sersic profiles to the three middle stellar mass bins of low concentration galaxies and to the four less massive bins of high concentration galaxies

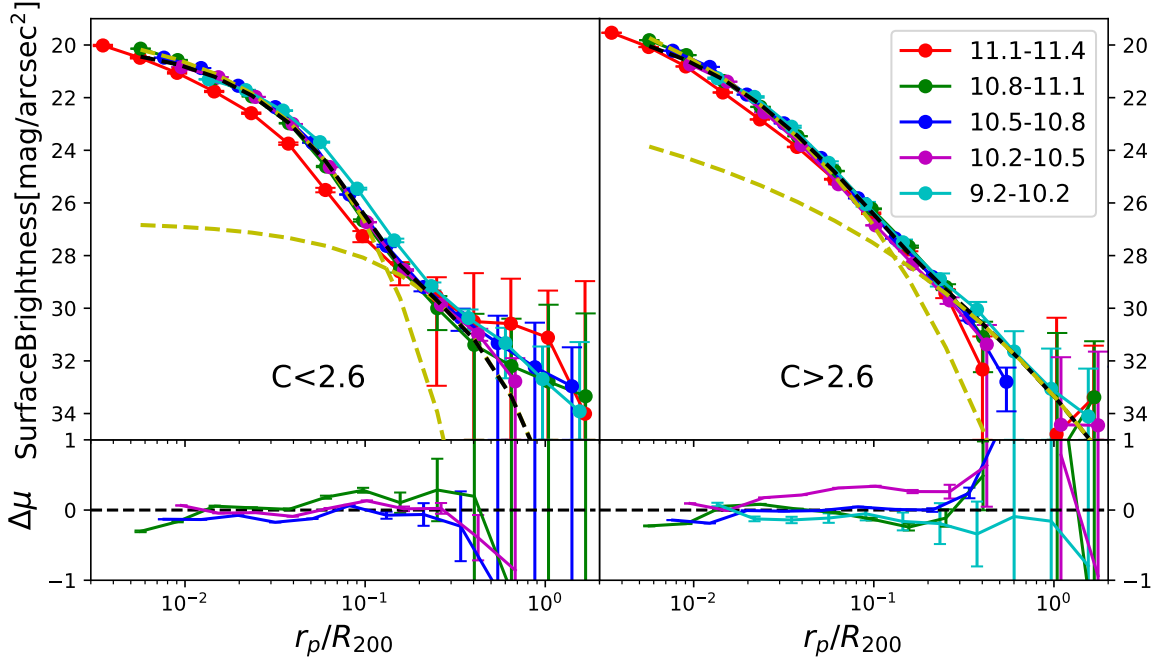


Figure 10. Top: Surface brightness profiles for low (left) and high (right) concentration galaxies in HSC r -band. The x -axis quantity is projected radial distance scaled by the halo virial radius. Black dashed lines are double Sersic models (PSF convolved), jointly fitted to the three middle bins ($10.2 < \log_{10} M_*/M_\odot < 11.1$) for low concentration galaxies and to the four less massive bins ($9.2 < \log_{10} M_*/M_\odot < 11.1$) for high concentration galaxies. Yellow dashed lines show the two best-fit Sersic components (not convolved by the PSF). Errorbars are boot-strap errors, which reflect the $1\text{-}\sigma$ scatter of galaxies within each stellar mass bin. **Bottom:** Difference between best fits and true surface brightness profiles of the few stellar mass bins used for fitting.

Table 3. Best-fit parameters of the double Sersic profile

	$C < 2.6$	$C > 2.6$
$I_{e,1}$	-8.7500 ± 0.0083	-8.5939 ± 0.0125
n_1	0.2583 ± 0.2248	2.5252 ± 0.0514
$x_{e,1}$	0.0049 ± 0.0016	0.0163 ± 0.0004
$I_{e,2}$	-11.59 ± 0.2466	-11.3881 ± 0.3816
n_2	1.1909 ± 0.948	3.7760 ± 1.0663
$x_{e,2}$	0.1775 ± 0.0472	0.1617 ± 0.0683

$$I/I_0 = 10^{I_{e,1}} \exp\{-b_{n_1}(x/x_{e,1})^{1/n_1} - 1\} + 10^{I_{e,2}} \exp\{-b_{n_2}[(x/x_{e,2})^{1/n_2} - 1]\}, \quad (1)$$

where we let $x = r_p/R_{200}$. $x_{e,1/2}$ is effective radius, scaled by the halo virial radius, R_{200} . $b_{n,1/2}$ is defined through $x_{e,1/2}$.

Again the model profiles are convolved with the typical PSF of each stellar mass bin. Measurements crossing different stellar mass bins are jointly used for the fitting. The best fits are presented as the black dashed lines, with the two Sersic components demonstrated as yellow dashed curves. The best-fit parameters and associated errors are provided in Table 3.

The residuals compared with the best fits are demonstrated in the lower panels of Fig. 10, for the few stellar mass bins used for fitting only. The colour legend is the same as

for top panels. The deviations from best fits are smaller than $0.15 \text{ mag/arcsec}^2$ within $0.3R_{200}$, except for the $10.2 - 10.5$ mass bin of high concentration galaxies. On scales larger than $0.3R_{200}$, the residuals increase significantly, reflecting the large scatter on such scales. For low concentration galaxies, adding a third Sersic component can help to improve the best fits on large scales (D'Souza et al. 2014), but given the large scatter and errors on such scales, we stick to two components. It is clear that the best fits tend to reconcile among measurements of different stellar mass bins, which are jointly used for the fitting. So we conclude that, although the profiles become very similar to each other after being scaled by R_{200} , discrepancies among different mass bins still remain. The discrepancies might be partly related to the fact that we have ignored K-corrections. Moreover, such discrepancies might be caused by uncertainties of R_{200} . More accurate determination of R_{200} has to depend on weak lensing measurements, and we will make further investigations in future studies. Lastly but importantly, we have ignored the scatter of the host halo mass distribution at fixed stellar mass, and the large scatter with respect to the mean halo mass versus stellar mass relation might be responsible for the discrepancies as well.

The fact that the surface brightness profiles of the stellar halo can be approximately modelled by the same functional form once scaled by the halo virial radius is very interesting. It indicates that, the formation of the faint outer stellar halo is likely to be dominated by physical processes that can be modelled through halo-related properties. How-

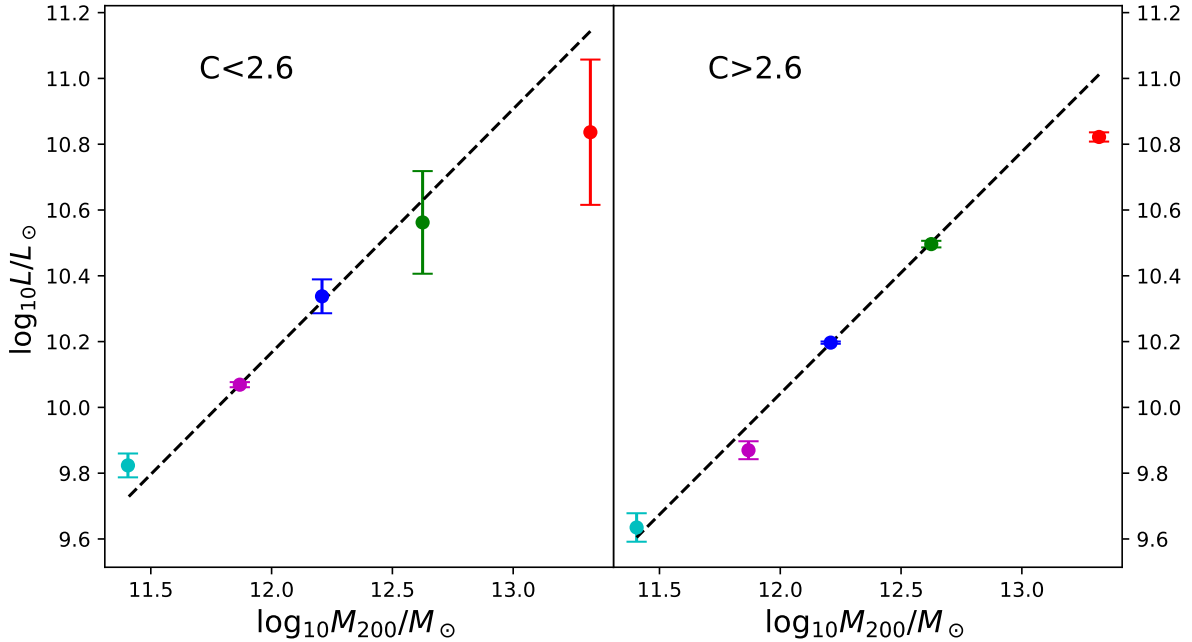


Figure 11. Integrated luminosity (out to the last positive data point of measured surface brightness profiles) versus the mean halo mass (based on a mock galaxy catalogue). Black dashed lines are best fits of $\log_{10} L/L_{\odot} \propto (0.7279 \pm 0.1887) \log_{10} M_{200}/M_{\odot}$ (left) and $\log_{10} L/L_{\odot} \propto (0.7346 \pm 0.0330) \log_{10} M_{200}/M_{\odot}$ (right). Only the three middle points on the left and the four less massive points on the right are used for fitting.

ever, the seemingly unified stellar halo profiles is only valid in terms of the "averaged" profiles for a large sample of galaxies. The slopes and masses of stellar haloes for individual galaxies show large diversities (e.g. [Harmsen et al. 2017](#); [Huang et al. 2018a](#)), reflecting the stochasticity of merging histories. Using the high-resolution Illustris simulation, [Pillepich et al. \(2014\)](#) investigated the logarithmic slopes of spherically averaged stellar density profiles for galaxies at $z = 0$. The slopes are at first measured for individual galaxies in a radial range of $R_{\text{vir}}/50$ to R_{vir} . While individual slopes show large radial-dependence and large galaxy-to-galaxy scatters, the median slopes show strong trends with halo mass. At fixed halo mass, the slopes also depend on the colour, morphology, age and stellar mass of galaxies. Our stacked surface brightness profiles show a strong dependence on galaxy type (low and high concentration subsamples), but there is no clear indication for the slope of averaged profiles to depend on stellar mass or halo mass for low concentration galaxies with $10.2 < \log_{10} M_{*}/M_{\odot} < 11.1$ and for high concentration galaxies with $9.2 < \log_{10} M_{*}/M_{\odot} < 11.1$. Over such stellar mass ranges the profiles are close to be universal on average.

In fact, if the universality of the stellar halo profiles strictly holds, it means that the luminosity should be proportional to $M_{200}^{2/3}$. The total luminosity is obtained through $L = \int I(r, R_{200}) 2\pi r dr$ or $L = \int I(x, R_{200}) 2\pi (xR_{200}) d(xR_{200})$, where $x = r/R_{200}$. Now, $I(r, R_{200})$ can be modelled as $I(x)$, i.e., the surface brightness profile only depends on $x = r/R_{200}$. Thus the integral of $L = \int I(x) 2\pi (xR_{200}) d(xR_{200})$ naturally leads to the conclusion that the luminosity, L , is proportional to

R_{200}^2 and hence $M_{200}^{2/3}$. The best-fit slopes of the integrated luminosity versus halo mass are 0.7279 ± 0.1887 for low concentration galaxies with $10.2 < \log_{10} M_{*}/M_{\odot} < 11.1$ and 0.7345 ± 0.0330 for high concentration galaxies with $9.2 < \log_{10} M_{*}/M_{\odot} < 11.1$, respectively (Fig. 11). The slopes are close to $2/3$. The most massive data point shows more significant deviation from the scaling relation. This is in very good agreement with [Yang et al. \(2008\)](#). [Yang et al. \(2008\)](#) measured the central galaxy luminosity versus halo mass relation through abundance matching of the SDSS galaxy group catalogue. They reported a best-fit relation of $L_C \propto M_h^{0.68}$ for $10^{11.6} h^{-1} M_{\odot} \leq M_h \leq 10^{12.5} h^{-1} M_{\odot}$, whereas for $M_h > 10^{12.5} h^{-1} M_{\odot}$, the slope is significantly flat. Both the best-fit slope and the halo mass range where the slope gets flattened are in very good agreement with our independent measurements here.

The halo mass of [Yang et al. \(2008\)](#) is obtained through abundance matching to the characteristic luminosity of galaxies in the SDSS group catalogue ([Yang et al. 2007](#)), and hence maybe the relation between halo mass and luminosity is a result from abundance matching. In addition, although R_{200} and M_{200} for our isolated central galaxy sample is not exactly obtained from abundance matching, it only slightly deviates from the abundance matching relation. Since stellar mass is strongly correlated with luminosity, the scaling between luminosity and halo mass might be a reflection of how M_{200} is determined. However, we emphasise that, we are able to self-consistently explain why the slope is close to the value of $2/3$, which cannot be deduced through abundance matching in an obvious way. With R_{200} mainly determined

through stellar mass and the aid of a mock galaxy catalogue, we are at least able to bring the stellar halo profiles for galaxies with a wide range of stellar masses to be close to universal.

5 DISCUSSIONS

5.1 Fraction of missing light

Single component models are often used to fit the surface brightness distribution of galaxy images, such as the de Vaucouleurs profile for elliptical galaxies and exponential profile for spiral galaxies. A pure de Vaucouleurs or a pure exponential model profile was used to fit galaxy images in SDSS, with the integrated flux called model magnitude. The fits are dominated by the central part of the galaxy, and hence for bright galaxies ($r < 18$), model magnitudes underestimate the total flux (e.g. [Strateva et al. 2001](#)). As a comparison, the composite model (cModel) fits a combination of de Vaucouleurs and exponential profiles to the observed surface brightness profiles of galaxies (Eqn. 2), which gives significant improvements in terms of modelling the total flux and also agrees well with the SDSS Petrosian magnitude

$$I_{\text{composite}} = \text{frac}_{\text{dev}} I_0 e^{-7.67(r/R_e)^{1/4}} + (1 - \text{frac}_{\text{dev}}) I_0 e^{-1.68(r/R_e)}. \quad (2)$$

Even though cModel magnitudes perform better in modelling the total flux, there might be missing light in outskirts of the faint stellar halo, which cannot be resolved given the background noise level of single images. Our stacked light profiles, however, are deeper than what can be obtained through individual images, and hence based on the stacks, we aim to test how cModel magnitude performs in very outer parts of the stellar halo, if the best fits are only achieved using measurements above the background noise level of single images.

The average background noise level of individual images is represented by the black horizontal lines in Fig. 7. We fit PSF convolved Eqn. 2 to data points above this level. To get the typical PSF of each stellar mass bin, we use the pipeline to return the PSF map at the center of each galaxy. The PSF maps are then weighted averaged in the same manner as for real galaxy images. The best fits are overplotted as dashed lines in Fig. 7. The fits are reasonably good in inner regions, and gradually drop below the true profiles on scales where the signal is lower than the background noise level of individual images. However, given the large errorbars in outskirts, most of the data points still marginally agree with the best fits.

Fractions of light that are below the background noise level are presented in Fig. 12 as triangles. We integrate the light profile out to the last data point of valid non-negative measurement. Though the volume in outer parts is larger, the fraction of unresolved light falling below the background noise level of individual images is on average subdominant compared with the total integrated light (10% to 20%). This is because the surface brightness profiles drop very quickly as a function of radius. The fraction is slightly lower for less concentrated galaxies on the left. The boot-strap errors or scatters are very large beyond 60 kpc for the three most

massive stellar mass bins of low concentration galaxies, and hence the propagated errors to Fig. 12 are large as well.

Red dots in Fig. 12 show the fraction of missing light if relying on the integration over the best-fit cModel profiles, compared with the true profiles. Both the best fits and the true profiles are integrated to the last data point of valid non-negative measurement. The extrapolation of cModel profiles helps to compensate part of the light under background noise level, so the fraction is lower than that of the triangles. Given the depth of HSC, it is encouraging that the missed fractions are below 10% except for the least massive bin. High concentration galaxies show slightly higher fractions of missing light, which is probably due to the higher fraction of accreted stars in outskirts of high concentration galaxies, with respect to the amount of stars formed in-situ through gas cooling (e.g. [D’Souza et al. 2014](#)).

5.2 Possible explanations for the positive colour gradients

We have shown in Sec. 4.1 and Sec. 4.2 that the measured $g - r$ and $g - i$ colour profiles of galaxies with $9.9 < \log_{10} M_*/M_\odot < 10.2$ show significantly redder colour or positive colour gradients beyond 30 kpc. There are also indications of a bump-like structure for galaxies with $10.2 < \log_{10} M_*/M_\odot < 10.5$, but the bump disappears for galaxies selected with more strict isolation criteria (Appendix C). The positive colour gradients have been reported by [D’Souza et al. \(2014\)](#), but our results are inconsistent with [D’Souza et al. \(2014\)](#) because the detected positive gradients in our results happen on different scales and for galaxies smaller than [D’Souza et al. \(2014\)](#).

The sample of galaxies used by [D’Souza et al. \(2014\)](#) are selected to be the brightest within 1 Mpc and 1000 km/s. We have repeated our analysis with galaxies selected by exactly the same criteria, and our results still lack in prominent positive gradients on similar scales as [D’Souza et al. \(2014\)](#). We provide details in Appendix C. It indicates that the disagreement is unlikely to be caused by the difference in sample selection.

It is natural to expect that the colour of galaxies is the reddest in the very central region, where the density is extremely high, the possible existence of black holes heats the surrounding gas and the disk instability triggers the formation of bulges. These processes can all potentially act to prohibit star formation activities. The feedback effect drops in the outskirts of galaxies and the amount of cold gas increases, which allows for more star formation activities and hence bluer colours.

On larger scales, the extended stellar halo is mainly built up through accretion of merged satellites in the current standard structure formation theory of our universe (e.g. [Oser et al. 2010](#); [Cooper et al. 2013](#)). After falling into the host halo, satellite galaxies undergo environmental effects such as tidal and ram-pressure stripping, which gradually remove their gas reservoir, i.e., the fuel for their star-formation activities. So there are less star formation in satellite galaxies than galaxies with comparable stellar masses in the field. However, the stripped stars could be a mixture of stars formed before falling into the host halo and newly formed stars after infall, and the merged population of satellites span a wide range of stellar mass at different

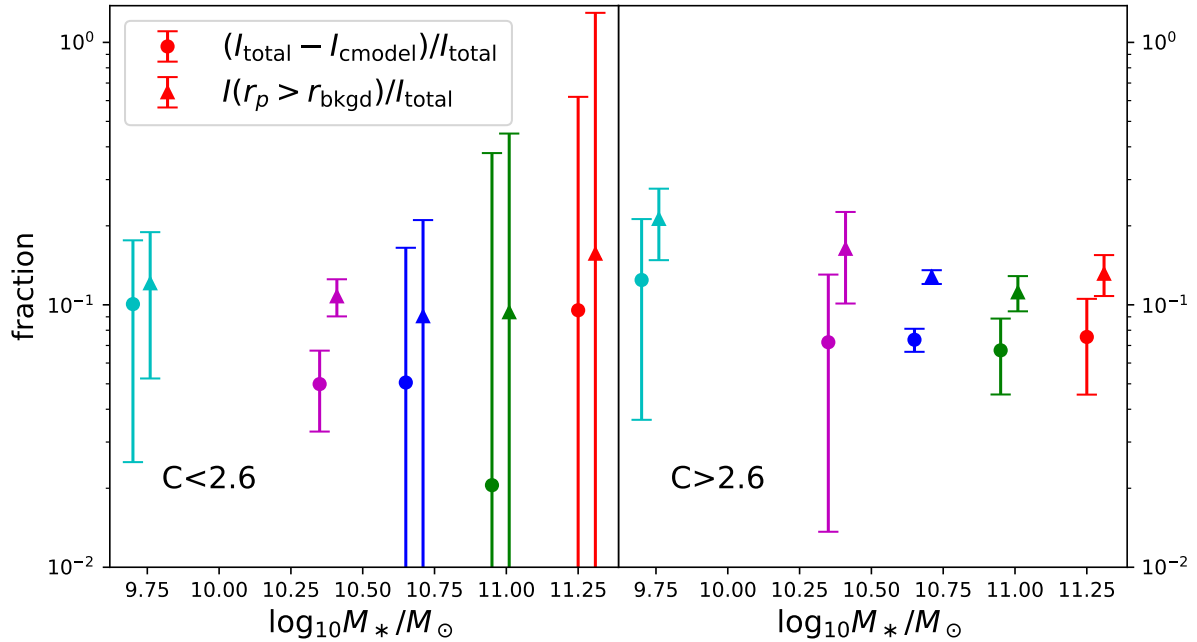


Figure 12. Round dots are the fractions of missing light based on cModel fits to HSC r -band surface brightness profiles above the average background noise level, and extrapolated to larger scales. Triangles are the fractions of light which are under the average background noise level. Left and right panels are for low and high concentration galaxies respectively.

epoches. It is hard to directly see from the picture whether the stellar halo should be redder than the outskirts of central galaxy or not. It is likely that because low concentration galaxies are bluer in the center, the contrast between the colour of central galaxies and the colour of surrounding stellar haloes is larger, and thus D’Souza et al. (2014) detected more obvious turning-up behaviours in the colour profiles of low concentration galaxies.

On the other hand, the positive gradients can be related to instrumental effects. For example, SDSS used thinned CCDs, and Michard (2002) pointed out that atmospheric seeing dominates the central part of the PSF, whereas in the outer regions, the PSF wings are controlled by both instrumental and atmospheric scattering. The extended wings of the red-band PSF are much brighter than that of bluer bands for thinned CCDs, which is called the “red halo” effect (e.g. Sirianni et al. 1998) that can possibly affect the colour in outer parts of bright objects. The red halo effect could be much less prominent as HSC uses thicker CCDs, which might explain why we fail to detect positive gradients on similar scales and mass ranges as D’Souza et al. (2014). This is supported by the fact that Huang et al. (2018a) looked at very massive galaxies with $\log_{10} M_*/M_\odot > 11.4$ at $0.3 < z < 0.5$ using HSC data, and their profiles show smooth negative colour profiles, consistent with many previous studies (e.g. Carollo et al. 1993; La Barbera et al. 2012).

Moreover, Wu et al. (2005) pointed out that the red halo effect is more prominent in SDSS i -band, and the extended PSF wings are expected to affect the surface brightness profiles of galaxies at radii larger than $10''$, which corresponds to about 12 to 20 kpc over the redshift range ($0.06 < z < 0.1$)

probed by D’Souza et al. (2014). The scales are roughly where the profiles measured by D’Souza et al. (2014) start to show positive colour gradients. Our sample of galaxies with $\log_{10} M_*/M_\odot > 10.2$ have higher redshifts than the sample of D’Souza et al. (2014), and thus a fixed angular scale corresponds to larger physical separations, but we still fail to detect positive gradients on such large scales for galaxies with $\log_{10} M_*/M_\odot > 10.2$. This supports the argument that the lacking in positive gradients in our results is unlikely caused by difference in the redshift, and is more likely because the red halo effect is less prominent for thicker CCDs. However, we note that both D’Souza et al. (2014) and our study measure the $g - r$ colour, for which the red halo effect could be less prominent.

Although we fail to detect positive colour gradients on similar scales and mass ranges as D’Souza et al. (2014), we cannot rule out the possibility that for galaxies with $9.2 < \log_{10} M_*/M_\odot < 10.2$ in our analysis, the red halo effect might still be responsible for the detected positive colour gradients. It is likely that the outskirts of these small and faint galaxies are more vulnerable to scattered light, which then contaminates the colour profiles.

In fact, beyond the CCD scattering-specific red halo effect, the scattering by atmospheric aerosols, dust and the reflection within the instrument/telescope can cause the so-called “aureole” (e.g. Sandin 2014) in the PSF on scales larger than the red halo. The aureole typically has size from a few tenth of arcsecond to about 1° . At $z = 0.07$ and $z = 0.05$, the corresponding physical scales for $30''$ are about 40 and 30 kpc. The scales are roughly consistent with the radius where we start to see flattened behaviours and

positive gradients in the colour profiles for galaxies with $9.2 < \log_{10} M_*/M_\odot < 10.2$. It is likely that because the mean redshift of these smaller galaxies are lower, they are more significantly affected by the aureole. For more massive galaxies at higher redshifts, probably the aureole mostly affects scales larger than the radial range probed in our current analysis.

Another possible source which might affect the colour measurements is related to the sky background subtraction. Measuring colour profiles for the extended faint stellar halo requires particular attention and extreme care to background subtractions. If the quality of background subtraction differs for different bands, the measured colour profiles based on coadd images are likely to be affected.

Despite these possible systematics, in case the positive gradients are real, it might be indicative of some distinct mechanisms which are ruling the gas cooling and star formation of these low mass galaxies. It has been known that low redshift galaxies can be divided into two populations of star-forming/disk dominated and quiescent/bulge dominated, with a transition stellar mass of about $10^{10.5} M_\odot$ (e.g. Kauffmann et al. 2003; Dekel & Birnboim 2006; Cattaneo et al. 2006). Galaxies lower than this transition stellar mass are typically younger, and mostly have low concentrations and low surface mass densities. Below the transition stellar mass of $10^{10.5} M_\odot$, we start to see indications of positive gradients in our measurements. However, given the existing theory of galaxy formation, it is difficult to propose a self-consistent picture or mechanism which can explain why the outskirts of galaxies with $9.2 < \log_{10} M_*/M_\odot < 10.2$ are systematically redder.

6 CONCLUSIONS

Stacking images of the Hyper Suprime-Cam Subaru Strategic Program Survey (HSC-SSP), we investigate the properties of faint stellar haloes centered on a sample of isolated central galaxies, which are the brightest within the projected halo virial radius and three times the virial velocity along the line-of-sight. Tested against a mock galaxy catalogue of the Munich semi-analytical model, we find above 85% of the isolated central galaxies are true central galaxies of dark matter haloes. We estimate and further subtract the residual background using similar stacks centered on a sample of random points, which are ideally flat and uniform.

The deep HSC images and the isolated central galaxy sample allow us to measure the average surface brightness profiles of galaxies spanning a wide range in stellar mass ($9.2 < \log_{10} M_*/M_\odot < 11.4$), and out to a projected radius of 120 kpc, with clear indications of signals extending further behind. The surface brightness in HSC r -band can be measured down to about $32.8 \text{ mag/arcsec}^2$.

More massive galaxies have brighter and more extended surface brightness, and redder colour profiles. The colour profiles are consistent with having negative gradients to about 80 kpc for galaxies with $10.2 < \log_{10} M_*/M_\odot < 11.4$. Less massive galaxies tend to have features of positive gradients beyond 30 kpc, but the errors are very large. The colour profiles of galaxies with $9.2 < \log_{10} M_*/M_\odot < 10.2$ are consistent with being flat on scales between 10 kpc and 30 kpc.

After further dividing galaxies into low and high concentration subsamples, we detect distinct features in their surface brightness and colour profiles. Low concentration galaxies are more flattened within 20 kpc, but their outer stellar halo profiles drop more quickly than high concentration galaxies between 20 kpc and 100 kpc. High concentration galaxies have redder and shallower colour gradients. These detections are in good agreement with D'Souza et al. (2014). However, we fail to detect positive gradients for low concentration galaxies on similar scales as D'Souza et al. (2014).

Very encouragingly, we can measure non-negative signals up to the halo virial radius for the surface brightness profiles of low concentration galaxies in HSC r -band, which are more extended beyond 100 kpc than high concentration galaxies. The virial radius is close to 500 kpc for galaxies with $11.1 < \log_{10} M_*/M_\odot < 11.4$. Despite the fact that the surface brightness profiles of individual galaxies show large scatters, we find the average surface brightness profiles can be modelled by a unified functional form, for low concentration galaxies with $10.2 < \log_{10} < 11.1$ and for high concentration galaxies with $9.2 < \log_{10} < 11.1$, after scaling the projected radius, r_p , by the halo virial radius, R_{200} . The discovery naturally leads to the conclusion that the total luminosity, L , of galaxies and the diffuse faint stellar halo scales with halo mass, M_{200} , in the manner of $L \propto M_{200}^{2/3}$, in very good agreement with Yang et al. (2008). The result also suggests that on top of the large scatter, the formation of stellar haloes in outskirts of galaxies can be on average modelled through physical processes that are likely universal once scaled by the host halo scale.

Stacking a large number of images enables us to push below the background noise level for individual images. We quantify the fraction of missing light based on the stacked surface brightness profiles which drop below the average background noise of single images in HSC. The fractions as a function of stellar mass are between 10% and 20% and are slightly higher for high concentration galaxies. We fit a composite model of exponential and de Vaucouleurs profiles (cModel) to measurements above the background noise of single images, and extrapolate to large scales to obtain the total integrated flux. Compared with the true measurements, the integrated cModel fluxes fall below the true measurements by fractions of less than or about 10%, but the errors associated the estimated fractions are very large due to the large scatter of the outer stellar halo.

Our results are robust to variations in the isolation criteria for sample selection and are robust to source detection thresholds used for creating masks. In addition, by using the single exposure images (Calex) of HSC, we add the pipeline subtracted background back and apply our own statistical background subtraction approach. We can validate the good performance of the pipeline in terms of removing the sky background and artificial instrumental features in the internal S18a data release.

ACKNOWLEDGEMENTS

Kavli IPMU was established by World Premier International Research Center Initiative (WPI), MEXT, Japan. This work was supported by JSPS KAKENHI Grant Num-

ber JP17K14271. WW is extremely grateful for extensive helps and discussions with Zhenya Zheng, Peter Draper, Shaun Cole, Nigel Metcalfe and John Lucy, which opened the door to image processing. WW is grateful for helps provided by John Good for details about image reprojection and the usage of Montage during the early stage of this paper, though in the end results are all decided to be based on the image resampling module of HSC pipeline instead of Montage. WW is also extremely grateful for useful email discussions with Richard D’Souza, and discussions with Chunyan Jiang, Jun Zhang and Chengze Liu.

REFERENCES

- Abazajian K. N., et al., 2009, *ApJS*, **182**, 543
- Aihara H., Arimoto N., Armstrong R., Arnouts S., Bahcall N. A., Bickerton S., Bosch J., Bundy K., 2018, *PASJ*, **70**, S4
- Anderson M. E., Gaspari M., White S. D. M., Wang W., Dai X., 2015, *MNRAS*, **449**, 3806
- Ann H. B., Park H. W., 2018, *Journal of Korean Astronomical Society*, **51**, 73
- Axelrod T., Kantor J., Lupton R. H., Pierfederici F., 2010, in *Software and Cyberinfrastructure for Astronomy*. p. 774015, doi:10.1117/12.857297
- Bell E. F., et al., 2008, *ApJ*, **680**, 295
- Blanton M. R., Roweis S., 2007, *AJ*, **133**, 734
- Blanton M. R., et al., 2005, *AJ*, **129**, 2562
- Bosch J., et al., 2018, *PASJ*, **70**, S5
- Buitrago F., Trujillo I., Curtis-Lake E., Montes M., Cooper A. P., Bruce V. A., Pérez-González P. G., Cirasuolo M., 2017, *MNRAS*, **466**, 4888
- Bullock J. S., Johnston K. V., 2005, *ApJ*, **635**, 931
- Callingham T., et al., 2018, preprint, (arXiv:1808.10456)
- Carollo C. M., Danziger I. J., Buson L., 1993, *MNRAS*, **265**, 553
- Cattaneo A., Dekel A., Devriendt J., Guiderdoni B., Blaizot J., 2006, *MNRAS*, **370**, 1651
- Chabrier G., 2003, *PASP*, **115**, 763
- Cooper A. P., et al., 2010, *MNRAS*, **406**, 744
- Cooper A. P., D’Souza R., Kauffmann G., Wang J., Boylan-Kolchin M., Guo Q., Frenk C. S., White S. D. M., 2013, *MNRAS*, **434**, 3348
- Cooper A. P., Gao L., Guo Q., Frenk C. S., Jenkins A., Springel V., White S. D. M., 2015, *MNRAS*, **451**, 2703
- Cunha C. E., Lima M., Oyaizu H., Frieman J., Lin H., 2009, *MNRAS*, **396**, 2379
- D’Souza R., Kauffman G., Wang J., Vegetti S., 2014, *MNRAS*, **443**, 1433
- Dekel A., Birnboim Y., 2006, *MNRAS*, **368**, 2
- Furusawa H., et al., 2018, *PASJ*, **70**, S3
- Greggio L., Falomo R., Scarpa R., 2018, *ApJ*, **861**, 81
- Guo Q., White S., Li C., Boylan-Kolchin M., 2010, *MNRAS*, **404**, 1111
- Guo Q., et al., 2011, *MNRAS*, **413**, 101
- Han J., Cole S., Frenk C. S., Jing Y., 2016, *MNRAS*, **457**, 1208
- Harmsen B., Monachesi A., Bell E. F., de Jong R. S., Bailin J., Radburn-Smith D. J., Holwerda B. W., 2017, *MNRAS*, **466**, 1491
- Hernández-Monteagudo C., Ma Y.-Z., Kitaura F. S., Wang W., Génova-Santos R., Macías-Pérez J., Herranz D., 2015, *Physical Review Letters*, **115**, 191301
- Huang S., Leauthaud A., Greene J. E., Bundy K., Lin Y.-T., Tanaka M., Miyazaki S., Komiyama Y., 2018a, *MNRAS*, **475**, 3348
- Huang S., et al., 2018b, *MNRAS*, **480**, 521
- Ibata R. A., et al., 2014, *ApJ*, **780**, 128
- Jee M. J., Tyson J. A., 2011, *PASP*, **123**, 596
- Jurić M., Kantor J., Lim K., Lupton R. H., Dubois-Felsmann G., Jenness T., Axelrod T. S., Aleksić J., 2015, preprint, (arXiv:1512.07914)
- Kado-Fong E., et al., 2018, preprint, (arXiv:1805.05970)
- Karademir G. S., Remus R.-S., Burkert A., Dolag K., Hoffmann T. L., Moster B. P., Steinwandel U., Zhang J., 2018, preprint, (arXiv:1808.10454)
- Kauffmann G., et al., 2003, *MNRAS*, **341**, 54
- Kawanomoto S., et al., 2018, *PASJ*, **70**, 66
- Komiyama Y., et al., 2018, *PASJ*, **70**, S2
- La Barbera F., Ferreras I., de Carvalho R. R., Bruzual G., Charlot S., Pasquali A., Merlin E., 2012, *MNRAS*, **426**, 2300
- Lackner C. N., Cen R., Ostriker J. P., Joung M. R., 2012, *MNRAS*, **425**, 641
- Li Z.-Z., Jing Y. P., Qian Y.-Z., Yuan Z., Zhao D.-H., 2017, *ApJ*, **850**, 116
- Lupton R., Blanton M. R., Fekete G., Hogg D. W., O’Mullane W., Szalay A., Wherry N., 2004, *PASP*, **116**, 133
- Malin D. F., Carter D., 1983, *ApJ*, **274**, 534
- Mandelbaum R., Wang W., Zu Y., White S., Henriques B., More S., 2016, *MNRAS*, **457**, 3200
- Martínez-Delgado D., et al., 2010, *AJ*, **140**, 962
- Michard R., 2002, *A&A*, **384**, 763
- Mihos J. C., Harding P., Feldmeier J., Morrison H., 2005, *ApJ*, **631**, L41
- Miyazaki S., Komiyama Y., Nakaya H., Kamata Y., Doi Y., Hamana T., Karoji H., Furusawa H., 2012, in *Ground-based and Airborne Instrumentation for Astronomy IV*. p. 84460Z, doi:10.1117/12.926844
- Miyazaki S., et al., 2018, *PASJ*, **70**, S1
- Monachesi A., et al., 2013, *ApJ*, **766**, 106
- Navarro J. F., Frenk C. S., White S. D. M., 1996, *ApJ*, **462**, 563
- Navarro J. F., Frenk C. S., White S. D. M., 1997, *ApJ*, **490**, 493
- Oser L., Ostriker J. P., Naab T., Johansson P. H., Burkert A., 2010, *ApJ*, **725**, 2312
- Peacock M. B., Strader J., Romanowsky A. J., Brodie J. P., 2015, *ApJ*, **800**, 13
- Pillepich A., et al., 2014, *MNRAS*, **444**, 237
- Planck Collaboration et al., 2013, *A&A*, **557**, A52
- Planck Collaboration et al., 2014, *A&A*, **571**, A16
- Planck Collaboration et al., 2016, *A&A*, **586**, A140
- Purcell C. W., Bullock J. S., Zentner A. R., 2007, *ApJ*, **666**, 20
- Rodríguez-Gomez V., et al., 2016, *MNRAS*, **458**, 2371
- Sales L. V., Wang W., White S. D. M., Navarro J. F., 2013, *MNRAS*, **428**, 573
- Sandin C., 2014, *A&A*, **567**, A97
- Schweizer F., 1980, *ApJ*, **237**, 303
- Schweizer F., Seitzer P., 1992, *AJ*, **104**, 1039
- Siriani M., et al., 1998, in *D’Odorico S., ed., Proc. SPIE Vol. 3355, Optical Astronomical Instrumentation*. pp 608–612, doi:10.1117/12.316832
- Spergel D. N., et al., 2003, *ApJS*, **148**, 175
- Staudaher S. M., Dale D. A., van Zee L., Barnes K. L., Cook D. O., 2015, *MNRAS*, **454**, 3613
- Strateva I., et al., 2001, *AJ*, **122**, 1861
- Tal T., van Dokkum P. G., 2011, *ApJ*, **731**, 89
- Tal T., van Dokkum P. G., Nelan J., Bezanson R., 2009, *AJ*, **138**, 1417
- Turkowski K., 1990, Academic Press Professional, Inc., San Diego, CA, USA, Chapt. Filters for Common Resampling Tasks, pp 147–165
- Wang L., Jing Y. P., 2010, *MNRAS*, **402**, 1796
- Wang W., White S. D. M., 2012, *MNRAS*, **424**, 2574
- Wang J., et al., 2011, *MNRAS*, **413**, 1373
- Wang W., Sales L. V., Henriques B. M. B., White S. D. M., 2014, *MNRAS*, **442**, 1363
- Wang W., White S. D. M., Mandelbaum R., Henriques B., Anderson M. E., Han J., 2016, *MNRAS*, **456**, 2301

- White S. D. M., Rees M. J., 1978, *MNRAS*, **183**, 341
 Wu H., Shao Z., Mo H. J., Xia X., Deng Z., 2005, *ApJ*, **622**, 244
 Yang X., Mo H. J., van den Bosch F. C., Pasquali A., Li C., Barden M., 2007, *ApJ*, **671**, 153
 Yang X., Mo H. J., van den Bosch F. C., 2008, *ApJ*, **676**, 248
 Zhao D. H., Jing Y. P., Mo H. J., Börner G., 2003, *ApJ*, **597**, L9
 Zhao D. H., Jing Y. P., Mo H. J., Börner G., 2009, *ApJ*, **707**, 354
 Zibetti S., White S. D. M., Brinkmann J., 2004, *MNRAS*, **347**, 556
 Zibetti S., White S. D. M., Schneider D. P., Brinkmann J., 2005, *MNRAS*, **358**, 949
 de Jong R. S., 2008, *MNRAS*, **388**, 1521
 van Dokkum P. G., Abraham R., Merritt A., 2014, *ApJ*, **782**, L24

APPENDIX A: A COMPARISON BETWEEN S15B AND S18A

A comparison of the stacked surface brightness profiles using coadd images of the S15b and S18a internal releases is provided in Fig. A1, following exactly the same image processing steps in Sec. 3. The horizontal dotted lines with triangle symbols are surface brightness profiles centered on random points. It is encouraging to see that the profiles are flat over the whole radial range. There is no excess light centered on random points, and thus our steps of processing images are successful. However, the random profiles are not exactly zero, which is positive for S18a and negative for S15b. It seems S15b suffers from over-subtraction in the sky background, while S18a has some small residual background remains.

Despite the possible over-subtraction and residual background, it is very encouraging to see that, on large scales (> 300 kpc), the surface brightness profiles centered on random points agree very well with the one centered on real galaxies (dashed lines with square symbols). The stacking centered on random points is a good estimate of the residual background, so we take the difference between profiles centered on real galaxies and random points to obtain final random corrected estimates of the surface brightness profiles (solid curves with round dots).

After random correction, the stack based on S15b end up with a prominent dip at $r_p \approx 100$ kpc, which is due to the over-subtraction of light in outskirts of massive bright objects, and it is very promising to see that the dip is absent in S18a. For S15b, we interpret the feature as possible over-fitting in the background, which is due to the high order adopted in the polynomial model used for background modelling (or equivalently the fitting scale). In comparison, the result based on S18a is significantly better (see Sec. 2.4), given that the green solid curve smoothly goes down to nearly zero without such a feature of dip.

APPENDIX B: COMPARISON WITH AN ALTERNATIVE BACKGROUND SUBTRACTION APPROACH

Throughout the paper, we use coadd images of the internal HSC S18a data release for our analysis. The sky background and instrumental features have been removed by the pipeline (Sec. 2.4). In this section, we apply an alternative statistical background subtraction approach to single exposure Calexp

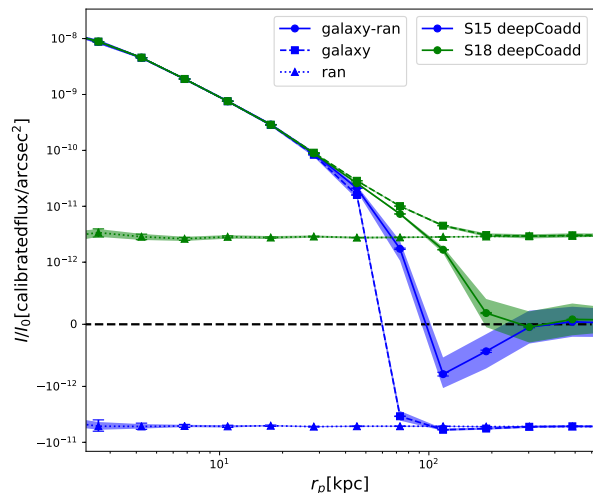


Figure A1. Stacked surface brightness profiles of isolated central galaxies with stellar mass in the range of $11.1 < \log_{10} M_*/M_\odot < 11.4$. Blue and green lines and symbols correspond to stacks based on S15b and S18a coadd images, respectively. For a given colour, solid line with dots, dashed line with squares and dotted line with triangles refer to the final random corrected surface brightness profile, the profile centered on real galaxies and on random points, respectively. The random sample is assigned exactly the same stellar mass and redshift distributions as real galaxies, in order to ensure exactly the same angular size distribution of extracted images. Errorbars are Poisson errors of photon counting. Shaded regions show the $1\text{-}\sigma$ scatter based on 100 boot-strap resampled realisations. The quantity of y -axis is intensity, I , divided by the corresponding zero point intensity, I_0 . To demonstrate negative values, y -axis regions with $I/I_0 > 10^{-12}$ and $I/I_0 < -10^{-12}$ are displayed in log scales for the absolute values, while the region of $-10^{-12} < I/I_0 < 10^{-12}$ is in linear scale. The black dashed horizontal line at $I/I_0 = 0$ is to guide the eye.

images of the internal S15b release¹¹ to test the robustness of our results to background subtraction and validate the internal S18a release. The Calexp images are produced after the first reduction step described in Sec. 2.3. For each single exposure image, we add the subtracted background model back and perform our own statistical background subtraction approach.

The general steps of processing coadd images and Calexp images are the same. We extract image cutouts centered on galaxies, dividing each by its zero point flux, resampling pixel values, correcting for cosmic dimming, creating masks by at first coadding all single exposures (visits) in HSC g , r and i -bands, and then masking companion sources for each band, clipping bad pixel values and stacking images. The

¹¹ Upon writing up this paper, the Calexp images of S18a have not yet released. Since the data reduction of correcting bias, flat field and dark flow is very similar for S15b and S18a, and our purpose of using Calexp images is to test the robustness of our results to possible variations of background subtraction, we focus on S15b Calexp images instead of spending more effort of waiting and reanalysing S18a Calexp images.

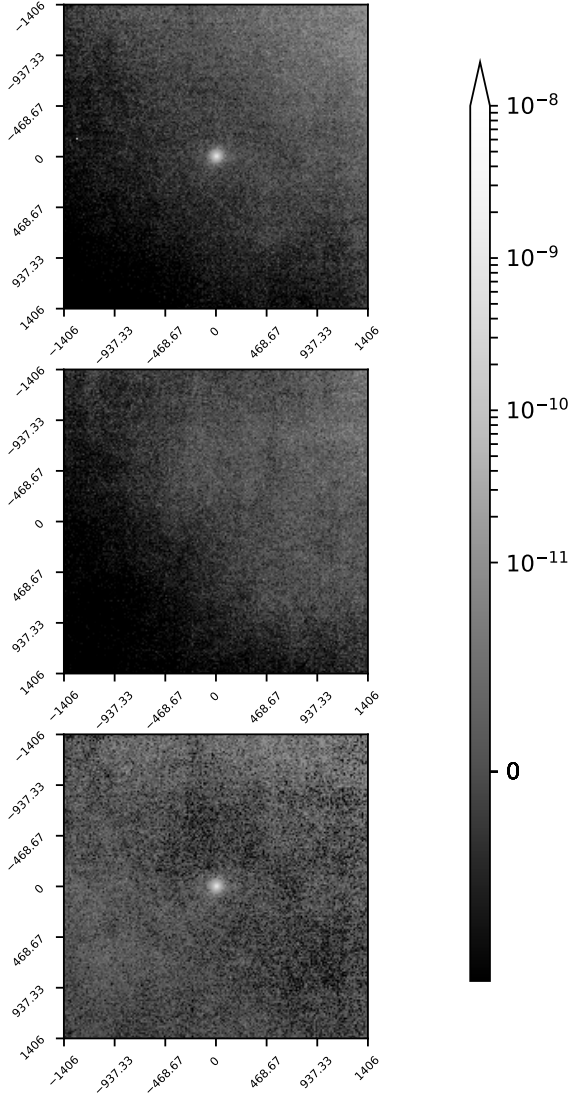


Figure B1. From top to bottom are stacked images (HSC r -band) centered on isolated central galaxies in the mass range of $11.1 < \log_{10} M_*/M_\odot < 11.4$, centered on random points, and the random corrected image, respectively. Pixel values are intensity divided by zero point intensity (I/I_0), i.e., $-2.5 \log_{10} I/I_0$ gives the surface brightness in unit of magnitude. The colour-map is exactly the same for the three panels, and is in log scale for $I/I_0 > 10^{-11}$ and linear for $I/I_0 < 10^{-11}$, in order to show negative pixel values. Image side length is roughly 2812 kpc.

main differences of processing the two sets of image products (and data releases) mainly come from the following aspects:

(i) A given sky region in HSC can be visited for multiple times. The pipeline has coadded all single exposure images together to create the coadd images. Thus for each galaxy in our analysis, it only corresponds to one given coadd image, so the number of galaxies and the number of coadd images are the same. For single exposure Calexp images, one galaxy may correspond to multiple images, and we have to stack all these single exposure images for a given sample of galaxies

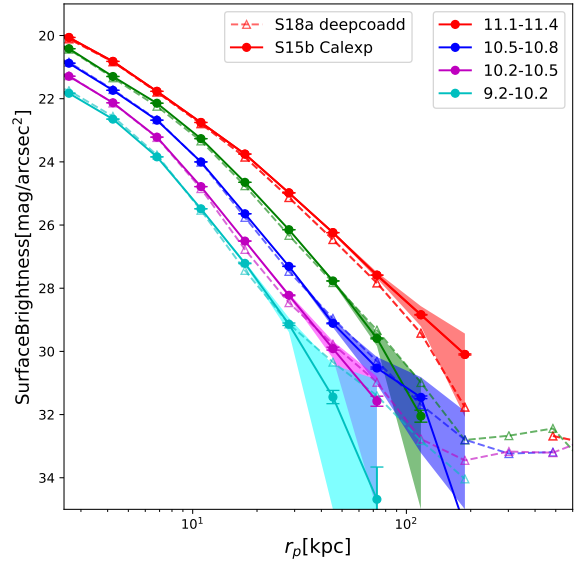


Figure B2. Dots connected by solid lines are surface brightness profiles in HSC r -band, based on S15b Calexp images and the statistical background subtraction approach. Errorbars are Poisson errors, and are mostly comparable to the symbol size except for the few outer most data points. Shaded regions show the $1\text{-}\sigma$ scatters of 100 boot-strap resampled realisations. Empty triangles connected by dashed lines are repeats of the results based on S18a coadd images (Fig. 5), for direct comparisons. The two least massive bins in Fig. 5 are combined together to achieve better signals.

together. The number of Calexp images is hence larger than the number of galaxies.

(ii) Using Calexp images, we have ignored the second joint calibration step of photometry and astrometry (see Sec. 2.3 for details). As have been stated, the source position accuracy after joint calibration is improved by about 25 mas, which is much smaller than the HSC pixel size ($0.17''$), so ignoring the joint calibration step will not significantly affect the science of this study.

(iii) The step of mosaic correction (Sec. 2.3) for the non-uniform flat field and for pixel area variations is not included for Calexp images, so we need to run the mosaic correction step at first.

(iv) We need to perform our own background subtraction.

We have taken into account all of the above differences in our analysis of S15a. In the following, we at first give a more detailed introduction of our approach to handle (iv), and then we move on to detailed comparisons between results based on S18a coadd images and S15b Calexp images.

As shown in Fig. 3, ring-like structures caused by the radial dependence of filter response curve over the CCD plate are mixed with the true sky background. We choose not to model and remove such patterns and the true sky background for individual images. Instead, we start with the resampled, cosmic dimming corrected and companion/foreground/background source masked image cutouts centered on galaxies (see Sec. 3 for more details), and for

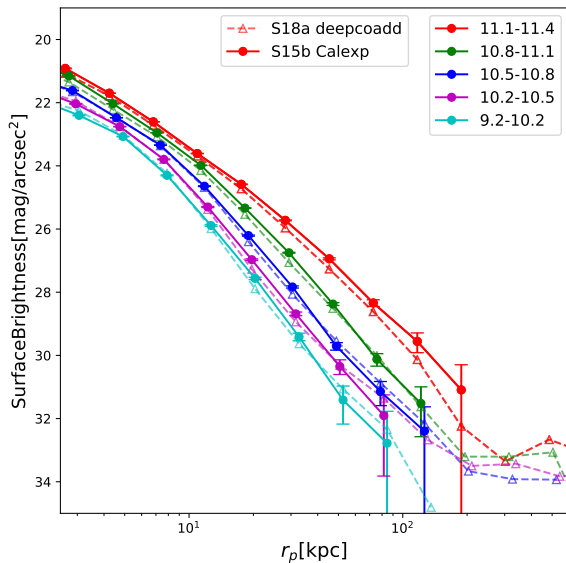


Figure B3. Similar to Fig. B2, but is based on HSC g -band. Since Poisson errors are much smaller than boot-strap errors, we only plot the scatters of 100 boot-strap resampled realisations as the errorbars. Small shifts along x have been added to the second to the least massive bins, to better display the errors.

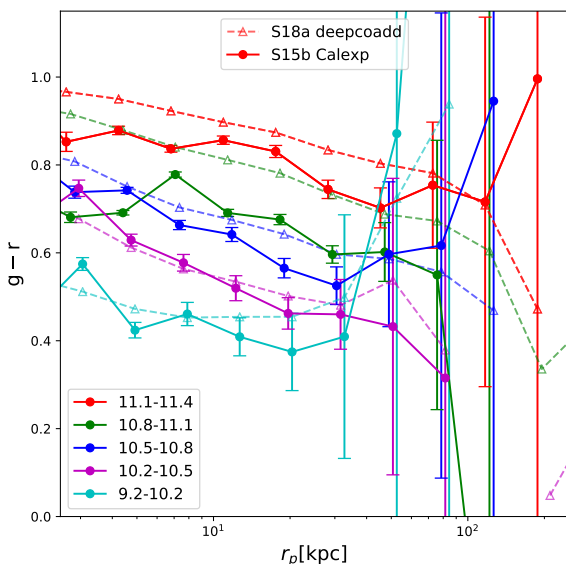


Figure B4. Dots connected by solid lines are $g-r$ colour profiles based on S15b Calexp images and the statistical background subtraction approach. Empty triangles connected by dashed lines are repeats of the results based on S18a coadd images (Fig. 6). Errorbars are $1-\sigma$ scatter based on 100 boot-strap realisations, and are only shown for S15b results. Small shifts have been added to x for the second to the least massive bins, to better display the errorbars.

each cutout, we at first estimate a mean value using unmasked pixels within an annulus of R_{200} and $3R_{200}$ from the galaxy or image center. This mean value is treated as an estimate of a constant background and subtracted off from the image. The true background is, however, not a constant, so the mean-subtracted images have both positive (for regions with higher background level) and negative (for regions with lower background level) pixel values. We assume that after stacking many different single exposure images, the background fluctuation/gradient can be averaged out. This would be the case when stacking an infinite number of images and in absence of any instrumental systematics.

In reality, the survey only covers a finite area, and the instrumental systematics as shown in Fig. 3 could potentially lead to a non-uniform residual when stacked over the survey footprint covered by our sample of isolated central galaxies. To correct for the remaining fluctuation/gradient in the final stack, we repeat exactly the same steps for a sample of random points. The random sample is forced to have exactly the same stellar mass and redshift distributions as that of real galaxies, but their sky coordinates are randomly shuffled within the survey footprint. If the pattern in Fig. 3 introduces a non-uniform background in the final stack, it is expected to be the same for both real galaxies and random points, because the sky coordinates of real galaxies should not be correlated with either true night sky background or instrumental patterns. The stacked images for real galaxies and random points in the stellar mass range of $11.1 < \log_{10} M_*/M_\odot < 11.4$ are shown in the two top panels of Fig. B1.

The large scale patterns for stacks around real galaxies and random points are very similar. They both show a gradient of being fainter in the lower left corner and brighter in the top right corner. This is mainly a result of the instrumental pattern in Fig. 3. To prove it, we spread a large realisation of random points over the plate of Fig. 3, and centered on each point, we extract a cutout, whose edge length is randomly drawn from the edge length distribution of our galaxies. We stack all the cutouts together, and the final stacked image shows a very similar gradient. Rotating images before stacking will help to “hide” such a gradient, but does not help to remove the residuals. So instead of rotating images, we correct the gradient using stacks around random points through the following equation:

$$\hat{I} = [I_g - I_r - \langle I_g(> R_{200}) - I_r(> R_{200}) \rangle] / I_{r,\text{shift}} \times \langle I_{r,\text{shift}} \rangle, \quad (\text{B1})$$

where I_g refers to the stacked image centered on real galaxies and I_r refers to the stacked image centered on random points. We take the difference between the real stack and the scaled random stack. This helps to account for the residual sky background. For Calexp images, we further correct for possible differences between the absolute sky background levels around real galaxies and random points using the term $\langle I_g(> R_{200}) - I_r(> R_{200}) \rangle$, which is the difference between stacks around real and random points, using the mean value of pixels outside a circle with radius of R_{200} . In the end, we divide the stack by $I_{r,\text{shift}} / \langle I_{r,\text{shift}} \rangle$. $I_{r,\text{shift}}$ refers to a shifted map of the final stacked image centered on random points, to which we have added the minimum value to the original map, $I_{r,\text{shift}} = I_r + \min(I_r)$. This is to make all pixel val-

Table B1. Total number of selected isolated central galaxies within the footprint of S15b internal data release.

$\log M_*/M_\odot$	N_{galaxy}
11.1-11.4	487
10.8-11.1	1825
10.5-10.8	1883
10.2-10.5	1121
9.2-10.2	883

ues positive. The division is very important. It helps to take away any possibly remaining fluctuations in the efficiency. However, our operation of adding the minimum pixel value may suffer from some arbitrariness, but since our purpose here is to make comparisons with results based on coadd images in the main text, we move on with the arbitrariness.

The random corrected image is shown in the bottom panel of Fig. B1. The large scale gradient is largely taken out. It is very promising because the images are not rotated before stacking. The sky background, however, still does not look ideally uniform, with some remaining fluctuations, but the pattern no longer shows any radial or angular dependence. Such a remaining pattern might be due to the unmasked extended light emission in outskirts of very bright objects and ghost images. Efforts have been devoted to the HSC pipeline to remove ghost images, the extended light emission and spikes around bright stars. Though in our analysis we have created multi-band stacked deep images at first and have adopted a low detection threshold of 0.8 times the background noise to create deep and extended masks for sources, including ghost images, some of the extended emission of very bright objects still remain. We have not achieved a very clean removal of these extended emissions for these Calexp images.

The stacked surface brightness profiles in HSC r -band, g -band and the $g-r$ colour profiles based on S15b Calexp images are presented in Fig. B2, Fig. B3 and Fig. B4. Results based on S18a coadd images in the main text are overplotted for direct comparisons. We only plot errorbars for S15b results to make clean figures. Results based on S15b Calexp images look less smooth and noisier. This is partly due to the fact that the sample size of S15b are nearly three times smaller (Table B1). (Note we combine galaxies with $9.9 < \log_{10} M_*/M_\odot < 10.2$ and $9.2 < \log_{10} M_*/M_\odot < 9.9$ together to a single stellar mass bin to achieve better signals for results based on S15b Calexp images.) Moreover, the less smooth results might be caused by the remaining extended light emission of very bright sources and ghost images, which might contaminate the final stacked surface brightness. Despite the noisier results, we can push to 200 kpc for the most massive bin, with smaller boot-strap errors and positive lower error boundary on that scale. For the other less massive bins, the largest scales we can reach is smaller than the results based on S18a coadd images.

Comparing S15b Calexp results with S18a coadd images, there are some discrepancies in detail. On large scales, S15b either drop more quickly or tend to be flattened (the most massive bin) than S18a, but the discrepancy is smaller or comparable to the large boot-strap errors on such scales.

This is likely due to the large fluctuation of the light distribution in outskirts of galaxies. On smaller scales, though the difference between S18a and S15b is much smaller in log-space, the difference is more significant compared with the small error size. This is especially true for the two most massive bins in HSC g -band and the $g-r$ colour profiles. We have explicitly tested that, the difference for the two bins only gets slightly reduced if comparing S15b Calexp images and S15b coadd images¹², so such a discrepancy cannot be explained by the difference in sky footprint or cosmic variance between the two data releases.

There are various possible reasons that might be responsible for such discrepancies. For example, as we mentioned above, the division of the term $\text{rans}_{\text{shift}}/\langle \text{rans}_{\text{shift}} \rangle$ in equation B1 involves some arbitrariness. In addition, for S18a coadd images, all single exposures centered on the same galaxy are stacked in the first hand by the pipeline, and then images centered on different galaxies are further stacked. On the other hand, S15b Calexp images are single exposure images, and we do mean background subtraction for each of them at first. Then we do clipping and weighted average all these single exposure images. The HSC pipeline did not involve any sigma-clipping as non-linear sigma clipping prevents the coadd image from having a well-defined effective PSF as pointed out by the pipeline paper (Bosch et al. 2018).

Except of these detailed disagreements which are likely caused by possible arbitrariness, assumptions in the statistical background subtraction approach and detailed differences between how coadd and Calexp images are stacked, the general agreement between the two sets of results is good in terms of both the shape and amplitude of the surface brightness and colour profiles. Our results are thus self-consistent and robust to the background subtraction, and it is encouraging to see the good performance of the pipeline in modelling and removing the background in S18a.

APPENDIX C: ROBUSTNESS OF OUR RESULTS TO VARIATIONS IN ISOLATION CRITERIA

Throughout the main text of this paper, the sample of galaxies are selected to be the brightest within the projected virial radius, R_{200} , and three times the virial velocity along the line-of-sight. This gives us a large sample, but the purity of halo central galaxies is about 85% at $9.2 < \log_{10} M_*/M_\odot < 11$. In this section we test our results using a sample of isolated central galaxies selected with more rigorous criteria and hence have significantly higher purity of halo central galaxies at $9.2 < \log_{10} M_*/M_\odot < 11$. This sample is selected to be the brightest within a projected distance of 1 Mpc and 1000 km/s along the line-of-sight.

The reader can find details about the purity and completeness for this sample in Mandelbaum et al. (2016). Basically, the 1 Mpc selection gives a sample purity that is above 90% for galaxies with $\log_{10} M_*/M_\odot < 10.8$. At

¹² Stacking S15b coadd images ends up with a prominent dip in the surface brightness profiles of bright galaxies (Fig. A1), but over the radial scales that are not affected by the dip, the agreement between measured surface brightness profiles based on S15b and S18a coadd images is very good.

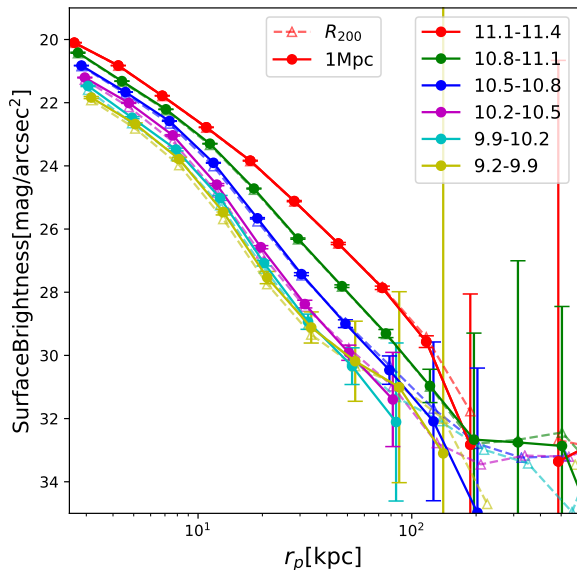


Figure C1. Solid lines and round dots are surface brightness profiles in HSC r -band for a sample of isolated central galaxies that are brightest within 1 Mpc and 1000 km/s along the line-of-sight. Errorbars are boot-strap errors based on 100 realisations. Empty triangles connected by dashed lines without errors are exactly the same as the measurements in Fig. 5, which are based on the sample of isolated central galaxies that are brightest within R_{200} and three times virial velocity along the line-of-sight, and are overplotted for direct comparisons. Small shifts have been added to x for the second to the least massive bins, to better display the errorbars.

Table C1. Total number of isolated central galaxies that are brightest within 1 Mpc in projected distance and 1000 km/s along the line-of-sight, and within the footprint of S18a internal data release.

$\log M_*/M_\odot$	N_{galaxy}
11.1-11.4	1318
10.8-11.1	3846
10.5-10.8	3232
10.2-10.5	1456
9.9-10.2	518
9.2-9.9	228

$9.2 < \log_{10} M_*/M_\odot < 10.$, the purity is nearly 100%, whereas the completeness is only about 40%. This is because the scale of 1 Mpc is larger than the mean halo virial radius at $\log_{10} M_*/M_\odot < 11.5$, and 1000 km/s is comparable to three times the mean virial velocity for galaxies with $\log_{10} M_*/M_\odot \sim 11.1$. Selecting galaxies with this more stringent criteria significantly helps to increase the sample purity at the small mass end.

Fig. C1 shows the stacked surface brightness profiles in HSC r -band for this sample, and results in the main text are overplotted for direct comparisons. The numbers of isolated central galaxies selected with the more strict criteria

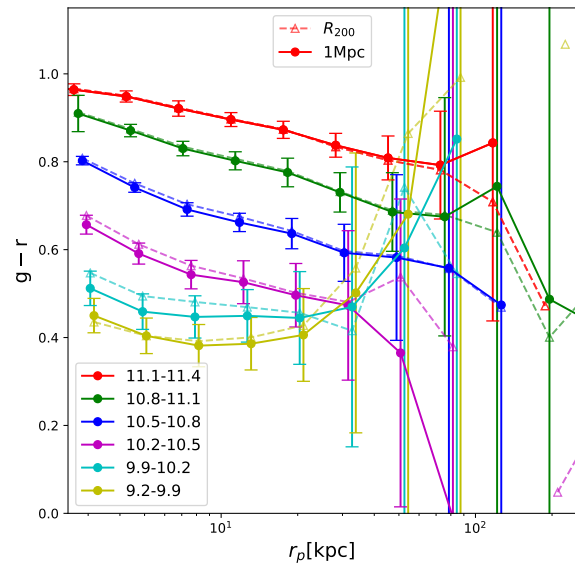


Figure C2. Solid lines and round dots are $g-r$ colour profiles for a sample of isolated central galaxies that are brightest within 1 Mpc and 1000 km/s along the line-of-sight. Errorbars are boot-strap errors based on 100 realisations. Empty triangles connected by dashed lines without errors are exactly the same as the measurements in Fig. 6, which are based on the sample of isolated central galaxies that are brightest within R_{200} and three times virial velocity along the line-of-sight. Small shifts have been added to x for the second to the least massive bins, to better display the errorbars.

and are within the S18a footprint are provided in Table C1. Compared with Table 1, the sample size is smaller by factors of 1.1, 1.3, 1.7, 2.3, 3.0 and 3.5 from the most to least massive stellar mass bins. The two samples are similar at the massive end. Solid and dashed lines for the two most massive bins are almost identical, but the discrepancy becomes slightly larger for smaller mass bins, for which the amplitudes of the surface brightness profiles are slightly higher in the more strictly selected sample. We checked this using the mock galaxy catalogue introduced in Sec. 2.1, and found more strictly selected isolated central galaxies tend to have slightly larger stellar masses and hence a bit higher amplitude in their surface brightness profiles.

Despite the small difference in the amplitude, the two sets of results are very similar in terms of their profile shape. The measured surface brightness profiles based on the R_{200} selected sample are more extended for the four less massive bins.

The colour profiles are provided in Fig. C2 for this new sample of isolated central galaxies, to be compared with the results in the main text (overplotted as dashed lines with empty triangles). The agreement is very good, except that for the fourth massive bin, the bump at $r_p \sim 50$ kpc disappears for the 1 Mpc selected sample, and the last points of the two most massive bins tend to turn up. On these scales the errorbars are very large. The existence of a positive gradient or bump-like structure in the fourth massive bin of Fig. 6 and the absence of the feature in Fig. C2 indicate

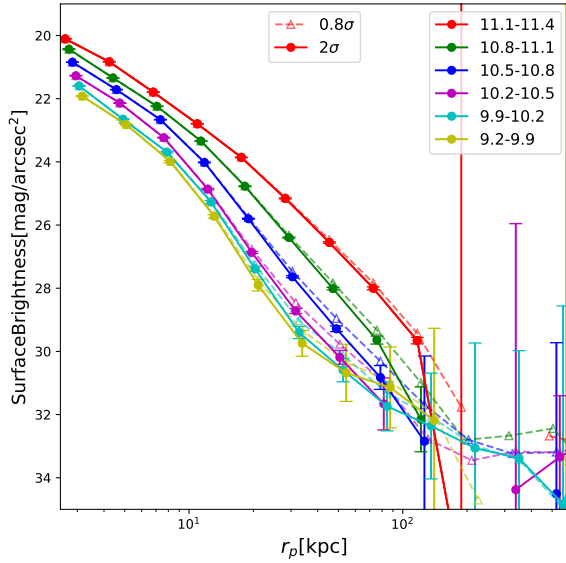


Figure D1. Solid lines and round dots are surface brightness profiles of galaxies in HSC r -band, obtained by masking companion and background sources using a detection threshold of 2σ the background noise. Empty triangles connected by dashed lines are exactly the same as the measurements in Fig. 5, which are based on masks created with a much lower source detection threshold of 0.8σ the background noise. Small shifts have been added to x for the second to the least massive bins, to better display the errorbars.

the positive gradient in this bin might be related to satellite contaminations or simply be statistical fluctuations. Despite the absence of the positive gradient in the fourth massive bin, the comparison indicates that satellite contamination due to less stringent selections of isolated central galaxies is unlikely to violate our results.

APPENDIX D: ROBUSTNESS OF OUR RESULTS TO VARIATIONS IN SOURCE DETECTION THRESHOLDS

As described in the main text, to create deep masks, we stack all visits in HSC g , r and i -bands, and then run SExtractor on the multi-band stacked images with a low detection threshold of 0.8 times the background noise. The low detection threshold helps to aggressively mask large segments associated with companions, foreground and background sources, but it also masks fake detections that might be background fluctuations. To check the effect of our source detection threshold, in this section we present results based on a less aggressive detection threshold, which is twice the background noise.

Results are shown in Fig. D1. Measurements obtained through the aggressively lower detection threshold (0.8σ) have slightly higher amplitude on large scales and are hence more extended. The low detection threshold helps to mask more light of sources, especially the extended emissions. Thus the residual background can be better estimated (see

Sec. 3.6 for details). The high detection threshold of 2σ , despite giving more robust source detections, the detected footprint of sources might not be large enough to cover the extended emission which should have been masked. As a result, the sky background is likely to have been over-estimated, which makes the results drop faster on large scales.